Elsevier Editorial System(tm) for Geochimica et Cosmochimica Acta

Manuscript Draft

Manuscript Number:

Title: The redox budget of crust-derived fluid phases at the slab-mantle interface

Article Type: Article

Corresponding Author: Dr. Nadia Malaspina,

Corresponding Author's Institution: Università degli Studi di Milano Bicocca

First Author: Nadia Malaspina

Order of Authors: Nadia Malaspina; Falko Langenhorst, Prof; Simone Tumiati, Dr; Marcello Campione, Dr; Maria Luce Frezzotti, Prof; Stefano Poli, Prof

Abstract: The redox processes taking place in the portion of the mantle on top of the subducting slab are poorly investigated and the redox potential of crust-derived fluids phases is still poorly constrained. A case study of supra-subduction mantle affected by metasomatism from crust-derived fluid phases is represented by garnet orthopyroxenites from the Maowu Ultramafic Complex (China) deriving from harzburgite precursors metasomatised at ~4 GPa, 750-800 °C by a silica- and incompatible trace element- rich fluid phase. This metasomatism produced poikilitic orthopyroxene and inclusion-rich garnet porphyroblasts. Solid multiphase primary micro-inclusions in garnet display negative crystal shapes and infilling minerals (spinel, ±orthopyroxene, amphiboles, chlorite, ±talc, ±mica) occur with constant modal proportions, indicating that derive from trapped solute-rich aqueous fluids. FT-IR hyper spectral imaging analyses and micro-Raman spectroscopy, together with X-Ray microtomography performed on single inclusions indicate that liquid water is still preserved at least in some inclusions (±spinel).
To investigate the redox budget of these fluid phases, we measured for the first time the Fe3+ concentration of the micron-sized precipitates of the multiphase inclusions using EELS on a TEM. Results indicate that spinel contains up to 12% of Fe3+ with respect to total iron, amphibole about 30%, while the ratio in inclusion phases such as chlorite and phlogopite may reach 70%. The Fe3+ fraction of the host garnet is equal to that measured in spinel as also confirmed by Flank Method EPMA measurements.
Forward modelling fO2 calculations indicate that the garnet orthopyroxenites record ΔFMQ=−1.8 ÷ −1.5, resulting apparently more reduced with respect to metasomatised supra-subduction garnet-peridotites. On the other hand, oxygen mass balance, performed both on the Maowu hybrid orthopyroxenite and on metasomatised supra-subduction garnet peridotites, indicate that the excess of oxygen (nO2) is the same (10 mol m-3). An oxygen mass balance of the crust-derived fluids (multiphase inclusions) also indicates that the fluid precipitates are more oxidised than the host rock, reaching up to 400 mol m-3 of nO2. This suggests that even after their interaction with the metasomatic orthopyroxenites, the residual fluid phases could be potentially carrier

of oxidised components when escaping the slab-mantle interface. Because of this gradient in nO2, a metasomatic front develops from the oxidised slab to the overlying lithospheric mantle wedge passing through a transitional layer of hybrid rocks at the slab-mantle interface.

Suggested Reviewers: Jörg Hermann
Institute of Geological Sciences, Universität Bern
joerg.hermann@geo.unibe.ch

Timm John
Institut für Geologische Wissenschaften, Freie Universität Berlin
timm.john@fu-berlin.de

Alan B. Woodland
Institut für Geowissenschaften, Goethe-Universität Frankfurt
woodland@em.uni-frankfurt.de

Baptiste Debret
Department of Earth Sciences, Durham University
ba.debret@gmail.com

Carmen Sanchez-Valle
Institut für Mineralogie, Universität Münster
sanchezm@uni-muenster.de

**Cover Letter**

UNIVERSITÀ DEGLI STUDI
DI MILANO - BICOCCA

DIPARTIMENTO DI SCIENZE DELL'AMBIENTE
E DEL TERRITORIO E DI SCIENZE DELLA TERRA

Milano, 5th October 2016

Dear Editor,

we are submitting to your attention the manuscript "**The redox budget of crust-derived fluid phases at the slab-mantle interface**" by N. Malaspina, F. Langenhorst, S. Tumiati, M. Campione, M. L. Frezzotti and S. Poli.

The paper is a study of orogenic metasomatised ultramafic rocks (garnet orthopyroxenites) associated with deeply subducted crust from the Maowu Ultramafic Complex (China) and provides information on fluid-mediated element transfer and redox processes occurring at the slab-mantle interface.

We aim to draw the attention to the controversial topic of the redox state attained in the mantle at subduction zones and the role of slab-derived high pressure fluid phases as carriers of oxidised components. Although it might be believed that the lithospheric mantle wedge above subduction zones is apparently more "oxidised" (i.e. records higher $fO_2$) as a result of metasomatism by slab-derived fluid phases, the debate about the process responsible for this relative oxidation and the actual oxidising capacity of slab-derived metasomatic fluids is still quite heated.

Slab-derived fluid phases are still preserved in the studied garnet orthopyroxenites within primary multiphase solid inclusions in garnets, as evidenced by the local occurrence of liquid water detected by high resolution Fourier Transform Infra Red imaging. To investigate the redox budget of these fluid phases, we measured for the first time the $Fe^{3+}$ concentration of the micron-sized precipitates of the multiphase inclusions by Electron Energy Loss Spectroscopy with the TEM. Results indicate that the solute content of deep slab fluids may contain very high $Fe^{3+}$ concentrations even after the interaction with the host garnet during the precipitation of the daughter phases.

We performed an oxygen mass balance between the fluid precipitates (up to 400 mol $m^{-3}$ of $nO_2$) and the host rock (10 mol $m^{-3}$ of $nO_2$), suggesting that even after their interaction with the metasomatic orthopyroxenites, the residual fluid phases could be potentially carrier of oxidised components when escaping the slab-mantle interface. We then modelled a gradient in $nO_2$ as a metasomatic front developing from the oxidised slab to the overlying lithospheric mantle wedge passing through a transitional layer of hybrid rocks at the slab-mantle interface.

This manuscript is based on original new data, ideas and interpretations. None of the submitted material has been published or is under consideration for publication elsewhere, including electronic media and databases.

All authors have seen the manuscript and agree to its submission to Geochimica et Cosmochimica Acta.

Yours faithfully

Nadia Malaspina, Falko Langenhorst, Simone Tumiati, Marcello Campione, Maria Luce Frezzotti and Stefano Poli

**Corresponding author:**

Dr. Nadia Malaspina (nadia.malaspina@unimib.it)
Dipartimento di Scienze dell'Ambiente e del Territorio e di Scienze della Terra
Università degli Studi di Milano Bicocca
Piazza della Scienza 4 – 20126 Milano (Italy)
Phone: (+39)0264482042 – Fax: (+39)0264482073

# The redox budget of crust-derived fluid phases at the slab-mantle interface

N. Malaspina[1*], F. Langenhorst[2], S. Tumiati[3], M. Campione[1], M. L. Frezzotti[1], S. Poli[3]

[1*] Dipartimento di Scienze dell'Ambiente e del Territorio e di Scienze della Terra, Università degli Studi di Milano Bicocca, Piazza della Scienza 4, 20126 Milano, Italy (nadia.malaspina@unimib.it; ph:+39 0264482042; fax: +39 0264482073)

[2] Institut für Geowissenschaften, Friedrich-Schiller Universität Jena, Burgweg 11, 07749 Jena, Germany

[3] Dipartimento di Scienze della Terra, Università degli Studi di Milano, via Mangiagalli 34, 20133 Milano, Italy

## Abstract

The redox processes taking place in the portion of the mantle on top of the subducting slab are poorly investigated and the redox potential of crust-derived fluids phases is still poorly constrained. A case study of supra-subduction mantle affected by metasomatism from crust-derived fluid phases is represented by garnet orthopyroxenites from the Maowu Ultramafic Complex (China) deriving from harzburgite precursors metasomatised at ~4 GPa, 750-800 °C by a silica- and incompatible trace element- rich fluid phase. This metasomatism produced poikilitic orthopyroxene and inclusion-rich garnet porphyroblasts. Solid multiphase primary micro-inclusions in garnet display negative crystal shapes and infilling minerals (spinel, ±orthopyroxene, amphiboles, chlorite, ±talc, ±mica) occur with constant modal proportions, indicating that derive from trapped solute-rich aqueous fluids. FT-IR hyper spectral imaging analyses and micro-Raman spectroscopy, together with X-Ray microtomography performed on single inclusions indicate that liquid water is still preserved at least in some inclusions (±spinel).

To investigate the redox budget of these fluid phases, we measured for the first time the $Fe^{3+}$ concentration of the micron-sized precipitates of the multiphase inclusions using EELS on a

TEM. Results indicate that spinel contains up to 12% of $Fe^{3+}$ with respect to total iron, amphibole about 30%, while the ratio in inclusion phases such as chlorite and phlogopite may reach 70%. The $Fe^{3+}$ fraction of the host garnet is equal to that measured in spinel as also confirmed by Flank Method EPMA measurements.

Forward modelling $fO_2$ calculations indicate that the garnet orthopyroxenites record $\Delta FMQ = -1.8 \div -1.5$, resulting apparently more reduced with respect to metasomatised supra-subduction garnet-peridotites. On the other hand, oxygen mass balance, performed both on the Maowu hybrid orthopyroxenite and on metasomatised supra-subduction garnet peridotites, indicate that the excess of oxygen ($nO_2$) is the same (10 mol $m^{-3}$). An oxygen mass balance of the crust-derived fluids (multiphase inclusions) also indicates that the fluid precipitates are more oxidised than the host rock, reaching up to 400 mol $m^{-3}$ of $nO_2$. This suggests that even after their interaction with the metasomatic orthopyroxenites, the residual fluid phases could be potentially carrier of oxidised components when escaping the slab-mantle interface. Because of this gradient in $nO_2$, a metasomatic front develops from the oxidised slab to the overlying lithospheric mantle wedge passing through a transitional layer of hybrid rocks at the slab-mantle interface.

**Keywords**

Flank method; Electron energy loss spectroscopy; Multiphase inclusions; Oxygen chemical potential; Oxygen fugacity; Subduction zone.

## 1. INTRODUCTION

The geochemical cycle of many light elements is deeply affected by the mutual stability of reduced or oxidised minerals and fluid species. Up to date, studies on the

52 oxidation state of the deep portions of the upper mantle have been concentrated on the
53 determination of oxygen fugacity ($fO_2$) in xenoliths of garnet peridotite samples from
54 subcratonic settings (Wood et al., 1990; Canil and O'Neill, 1996; Simakov, 1998;
55 McCammon et al., 2004; Woodland et al., 2006; Frost and McCammon, 2008; Creighton et
56 al., 2009; Yaxley et al., 2012; Hanger et al., 2015). On the contrary, the oxidation state of the
57 upper mantle at subduction zones, at the pressures corresponding to sub-arc depths, is still
58 poorly investigated (Malaspina et al., 2009b; 2010; 2012). With respect to garnet peridotite
59 continental xenoliths from the sub-cratonic mantle, garnet peridotites from subduction zones
60 record much higher oxygen fugacities with differences of 3-4 log units (Malaspina et al.,
61 2010). Although it might be believed that the lithospheric mantle wedge above subduction
62 zones is apparently more "oxidised" (i.e. records higher $fO_2$) as a result of metasomatism by
63 slab-derived fluid phases, the dispute about the process responsible for this relative oxidation
64 and the actual oxidising capacity of slab-derived metasomatic fluids is still going on (Brandon
65 and Draper, 1996; Frost and Ballhaus, 1998). Kelley and Cottrell (2009) studied the redox
66 condition of arc-magma sources from the $Fe^{3+}/\Sigma Fe$ analyses of lavas and melt inclusions from
67 arc volcanoes. These authors reported a linear correlation between $Fe^{3+}/\Sigma Fe$ ratios, $H_2O$
68 content and slab-derived fluid mobile elements, indicating that the oxidation state of such
69 magmas is closely related to subduction fluid influx in their source. If pure water is not likely
70 an efficient carrier of $Fe^{3+}$ (Schneider and Eggler, 1986), solute-rich slab-derived fluids could
71 be potentially able to mobilise $Fe^{3+}$ (Kelley and Cottrell, 2009) as shown for other trivalent
72 fluid-immobile elements such as REE (Kessel et al., 2005; Tsay et al., 2014).

73 The slab-mantle interface is therefore a key location where fluid-mediated element
74 transfer and redox processes must occur (Hirschmann, 2009). Information on such processes
75 can be gained by the study of orogenic metasomatised ultramafic rocks associated with deeply
76 subducted crust. Most of these garnet peridotites provide evidence of recycling in the mantle

of slab-derived fluids by the occurrence of primary multiphase solid inclusions, which have been attributed to silicate-rich supercritical liquids (Van Roermund and Carswell, 2002; Malaspina et al., 2006; Vrijmoed et al., 2006; Scambelluri et al., 2008; Malaspina and Tumiati, 2012; Frezzotti and Ferrando, 2015). These inclusions are hosted in minerals stable at high pressure (e.g. garnet), and show the same textural features as fluid inclusions. Their study thus enables to capture a snapshot of the nature and composition of the fluid phase, and its behaviour during the interaction with mantle peridotites.

A relevant case study is represented by garnet orthopyroxenites from the Maowu Ultramafic Complex, Dabie Shan, China. They form hybrid layers deriving from harzburgite precursors metasomatised at ~4 GPa, 750-800 °C by a silica- and incompatible trace element-rich fluid phase, subsequently preserved in primary multiphase solid inclusions. We analysed for the first time the $Fe^{3+}/\Sigma Fe$ content of the mineral infillings by Electron Energy Loss Spectroscopy (EELS) with the Transmission Electron Microscope (TEM), in order to investigate the redox budget of these fluid phases after the interaction with mantle peridotites.

## 2. PETROLOGICAL BACKGROUND

We selected a set of samples consisting of well-characterised garnet websterites and orthopyroxenites from the Maowu Ultramafic Complex (Dabie Shan, Eastern China). This body is formed by a layered sequence of meta-harzburgites, garnet orthopyroxenites and websterites associated with coesite-bearing eclogites. All these ultramafic rocks are locally bounded by phlogopite-rich layers (Malaspina et al., 2006) and are hosted by garnet-coesite-bearing gneisses. In this terrane, gneisses and ultramafic rocks share a common metamorphic history reaching peak conditions at 4-6 GPa and 750-800 °C during the collision between the Sino-Korean and Yangtze cratons in the Triassic (Zhang et al., 1995; Xue et al., 1996; Liou

and Zhang, 1998; Ayers et al., 2002; Jahn et al., 2003). The orthopyroxenites are strongly foliated, with centimetre-thick layers of oriented orthopyroxene and garnet-rich layers. The orthopyroxene-rich layers contain coarse orthopyroxene ($Opx_2$), which forms at the expense of a previous ultramafic assemblage made of fine-grained olivine, orthopyroxene ($Opx_1$), garnet ($Grt_1$) and rare clinopyroxene. Garnet-rich layers are composed by mm-sized zoned garnet ($Grt_2$), which includes core clusters of primary multiphase inclusions (Malaspina et al., 2015, 2006; Malaspina et al., 2009a). Previous studies by Malaspina et al. (2006; 2009a) demonstrated that the Maowu orthopyroxenites may represent a proxy for metasomatic layers at the slab/mantle interface, produced after the reaction of mantle peridotites with a Si-saturated liquid sourced from the associated crustal rocks at UHP conditions (4.0-5.0 GPa, 700-800 °C). As shown in Figure 1 and demonstrated by recent experimental results (Wang et al., 2016), a Si- and incompatible elements-rich liquid produced by the subducting crust is potentially very reactive when entering the supra-subduction mantle rocks. It may result in the formation of orthopyroxenites at the slab-mantle interface (Scambelluri et al., 2006; Endo et al., 2015). Petrographic evidence is recorded by the Maowu ultramafic rocks, where the olivine + $Opx_1$ + $Grt_1$ ± clinopyroxene mineral association of a previous harzburgite was replaced by poikiloblastic $Opx_2$ + $Grt_2$ after the reactive flow of crust-derived metasomatic agents (red arrows of Fig. 1). Part of the $H_2O$ component of the metasomatic liquid evolves into a residual aqueous fluid (blue arrows of Fig. 1) and concentrates the most incompatible elements (LILE, LREE). The primary multiphase inclusions hosted by $Grt_2$ cores were interpreted to derive from the precipitation of the solute content of this residual aqueous fluid (Malaspina et al. 2006, 2009a). Experimental homogenisation of these inclusions at conditions close to the estimated metamorphic peak (3.5 GPa and 800 °C) demonstrated that the multiphase inclusions derived from a solute-rich aqueous fluid trapped at supercritical conditions (Malaspina et al., 2006).

127 The analyses of the trace element composition of the multiphase inclusions of
128 orthopyroxenite samples from Maowu give information on the composition of such a residual
129 fluid. The trace element pattern of the fluid is shown in Figure 2 (pink area) and is
130 characterised by enrichment of LREE and a selective enrichment in LILE, with spikes of Cs,
131 Ba, and Pb relative to Rb and K. An important aspect of the filtering process described above
132 is that the residual fluid equilibrates with the mantle phases and is therefore able to travel and
133 metasomatise the supra-subduction mantle once it escapes the slab.
134 The studied samples will be compared with mantle-derived garnet peridotite from the
135 Sulu UHP terrane (Eastern China). These rocks correspond to a slice of supra-subduction
136 lithospheric mantle wedge (Zhang et al., 2000), which records a multistage metasomatism by
137 an alkali-rich silicate melt at high temperature, crystallising coarse phlogopite ($Phl_1$), garnet
138 and clinopyroxene ($Cpx_1$) in equilibrium with olivine and orthopyroxene, and a subsequent
139 influx of a slab-derived C-bearing fluid, enriched in incompatible elements, at lower
140 temperature, forming a second generation of phlogopite ($Phl_2$), garnet and clinopyroxene
141 ($Cpx_2$) together with magnesite (Malaspina et al., 2009a; Malaspina et al., 2009b). As
142 demonstrated by Malaspina et al. (2009a) and shown in Figure 2, $Phl_2$ trace elements analyses
143 (white triangles) show strong enrichments in LILE and complementary pattern of the other
144 incompatible elements with respect to $Cpx_2$ (dark diamonds), indicating equlibrium
145 partitioning. $Cpx_2$ shows a pronounced positive Pb anomaly and a relatively depleted pattern
146 in LILE with the same selective "W-type" LILE enrichment of the slab-derived fluid,
147 represented by the Maowu multiphase inclusions (Fig. 2). Figure 2 also shows, for
148 comparison, the incompatible trace elements pattern of amphibole-bearing garnet peridotite
149 from the Ulten Zone (Italian Alps), a well known example of supra-subduction mantle
150 peridotites metasomatised by crust-derived fluid phases (Tumiati et al., 2003; Scambelluri et
151 al., 2006; Tumiati et al., 2007). The similarity between the residual fluid trapped in the

inclusions of the Maowu rocks and the metasomatic pattern recorded by $Phl_2$ and $Cpx_2$ of the garnet peridotite from Sulu, along with the bulk rock composition of the Ulten peridotite, strongly suggests that this kind of fluids may be effective metasomatic agents in the lithospheric mantle wedge, once they escape the slab–mantle interface.

## 3. ANALYTICAL METHODS

### 3.1. Electron microprobe analyses and Flank Method

The $Fe^{3+}/\Sigma Fe$ of garnets, measured by the flank method with a wavelength dispersive system, was acquired with the JEOL 8200 Superprobe at the Department of Earth Sciences, University of Milano (Tab. 1). Flank method and quantitative elemental analyses were performed with wavelength-dispersive spectrometers at 15 kV and 60 nA. One spectrometer equipped with a TAP crystal and a 300 μm slit was used for the flank method, measuring the FeLβ and FeLα peaks for counting times of 300 s. With the remaining 4 spectrometers, $SiO_2$, $TiO_2$, $Al_2O_3$, $Cr_2O_3$, FeO, MgO, MnO and CaO were measured simultaneously. Natural silicates were used as standards: Mg–Al–Si on pyrope, Fe on almandine, Ca on grossular, Mn on rodonite, Cr on chromite and Ti on Ti-ilmenite. A PhiRhoZ routine was used for matrix correction. The quantitative $Fe^{3+}/\Sigma Fe$ measurements in garnet were determined by applying the correction for self-absorption (see Hofer and Brey, 2007 for details), using natural and synthetic garnet end-members with fixed $Fe^{3+}/\Sigma Fe$ as standards (Malaspina et al., 2012, 2010; Malaspina et al., 2009b).

Major element concentrations of the inclusions mineral infillings (Tab. 1) were analysed by wavelength dispersive spectrometry using a Jeol 8200 Super Probe at the Dipartimento di Scienze della Terra, University of Milano. Acceleration voltage was set to 15

177 kV, beam current was 15 nA and natural minerals were used as standard. Due to the very fine
178 size and to the limited exposure of the inclusions on the sample surface, it was difficult to
179 perform accurate quantitative analyses with the microprobe. Therefore we also measured
180 energy-dispersive X-ray emission spectra (EDX) on the transmission electron microscopy
181 (TEM, see below).
182
183 **3.2. Analytical Transmission Electron Microscopy**
184
185 Polished thin sections of orthopyroxenite samples were used for the preparation of
186 TEM foils. 3 mm wide Cu grid were glued onto areas of interest and then thinned to
187 perforation by Ar ion milling in a Gatan Duomill characterisation at 4.5 kV and an incidence
188 angle of 13°. TEM foils were imaged by conventional (bright-field and dark-field, Fig. 3B)
189 and high-resolution (Fig. 3C) techniques using a Philips CM20 FEG transmission electron
190 microscope at the University of Bayreuth.
191 EDX spectra were acquired to obtain compositions of the very small mineral
192 inclusions using a ThermoNoran Ge detector attached to the TEM. These analyses were
193 quantified on the basis of the principle of electroneurality by taking into account an
194 absorption correction (van Cappellen and Doukhan, 1994; Langenhorst et al., 1995) and the
195 $Fe^{3+}/\Sigma Fe$ ratios measured by electron energy loss spectroscopy (EELS).
196 EELS, employed to analyse orthopyroxene, garnet and inclusions infillings phlogopite,
197 amphibole, chlorite and spinel (Fig. 4), was carried out using a Gatan PEELS 666 mounted to
198 the TEM. The quantification of $Fe^{3+}/\Sigma Fe$ ratios was based on the white line intensities of the
199 Fe $L_{23}$ edges, which are well calibrated for garnets (van Aken et al., 1998). Fe $L_{23}$ electron
200 energy-loss near-edge structure (ELNES) spectra were acquired in diffraction mode with
201 convergence and collection semi-angles of $\alpha$=8 mrad and $\alpha$=2.7 mrad and an energy

dispersion of 0.1 eV per channel. The energy resolution, measured as width of the zero-loss peak at half maximum, was 0.8-0.9 eV. To test for possible beam-induced oxidation of the sample, six spectra were measured in a time series with integration times of 10 s each. Spectra were then corrected for dark current and channel-to-channel gain variation. To extract the pure single-scattering core-loss signal, an inverse power-law background was subtracted and multiple-scattering contributions were removed by the Fourier-ratio technique. Errors in the $Fe^{3+}/\Sigma Fe$ ratio are usually estimated to be on the order of 0.05, if the iron concentration is larger than 5 wt.% (van Aken et al., 1998; Frost and Langenhorst, 2002).

### 3.3. Fourier Transform Infra Red imaging and micro-Raman spectroscopy

FT-IR hyper spectral imaging analyses were performed using Agilent Cary 620. This instrument uses a 128 × 128 focal plane array (FPA) detector that enables to simultaneously collect all the spectra required for the map. Maps were collected in transmission mode on a 50 µm-thick double polished thin section, using 15× IR/Visible all-reflecting on-axis Schwarzchild objective (NA=0.62, working distance=21 mm) at 8 $cm^{-1}$, performing 32 scans per spectrum in the 3900 – 900 $cm^{-1}$ spectral range. Data were elaborated using the Agilent Resolution Pro software. $H_2O$ distribution has been extracted after computing the area of the $H_2O$ bending mode at 1630 $cm^{-1}$.

Raman spectra were collected with a LABRAM HRVIS (Horiba Jobin Yvon Instruments) at the Interdepartmental Center “G. Scansetti” (Department of Earth Sciences, University of Torino, Italy). The excitation source is a 532 nm solid-state Nd laser, with power at the emission source of 100 mW. Daily calibration was performed using the 520.6 $cm^{-1}$ Si band. Analyses were preformed inside fluid inclusions with a HR confocal set up, with resulting spot size of 1×1×3 µm. Spectral accumulations varied from 20 to 60 sec, and

three accumulations per spectrum were recorded. The positions of Raman bands were determined by fitting Gaussian/Lorenzian curves to the Raman spectra with Fityk 0.9.8 free software. Peak attribution has been based on our database of references spectra (e.g., Frezzotti et al., 2012).

### 3.4. X-Ray computed micro-tomography

The fragment of sample MWF2A was used as such for the X-ray micro-tomography analysis using a Skyscan 1172 high resolution microCT, at the CRIST center, Centro di Cristallografia Strutturale, of the University of Firenze. This system has a sealed, microfocus tungsten X-ray tube with a 5mm focal spotsize. X-rays were produced by exposing the anode to an electron beam at 100 kV and 100 mA. The sample was placed on the pedestal between the X-ray source and the CCD detector. The 2D X-ray images were captured over 180°, rotating the sample with a slice-to-slice rotation angle of 0.2°, each 2D image represents one slice. Spatial resolution time was 1.6 mm in terms of pixel size.

The 3D images of the objects have been reconstructed using modified Feldkamp algorithm for cone-beam acquisition geometry realized in Nrecon 1.6.9.4 software. The alignment, beam hardening and ring artifacts were corrected before starting reconstruction process. CTan software was used for the image clean up and CVol or CVox for the 3D visualization.

## 4. RESULTS

### 4.1. Mineral chemistry and $Fe^{3+}$ measurements of garnets and inclusion infillings

252 The major element compositions of garnets and minerals crystallised in the multiphase
253 inclusions of websterite (RPC171) and orthopyroxenites (MWF2 – MWF2A) from the
254 Maowu Ultramafic Complex are reported in Table 1. Representative analyses of
255 orthopyroxene from the same samples are also reported.
256
257 *4.1.1. $Fe^{3+}$ in garnet*
258 Garnets from the Maowu Ultramafic Complex show different compositions in terms of
259 $Cr_2O_3$, $Fe_2O_3$, MgO and CaO (Tab. 1). Average $Fe^{3+}/\Sigma Fe$ ranges between 0.05 and 0.07,
260 corresponding to ~1-1.5 mol% of skiagite ($Fe_3^{2+}Fe_2^{3+}Si_3O_{12}$) component. Garnets from
261 websterite sample RPC171 have lower pyrope and higher almandine, grossular and skiagite
262 contents, with respect to garnets from orthopyroxenites, which show average
263 $Py_{71}Alm_{23}Gro_5Ski_1$ composition. In Figure 5 all garnets show a negative correlation between
264 Al and $Fe^{3+}$ and define a trend of broad increase of $Fe^{3+}$ from orthopyroxenites to websterite
265 samples. Data from Maowu samples are compared with garnet compositions from Sulu
266 phlogopite-magnesite-bearing peridotite (Tab. 1 and Fig. 5) and with garnets from Ulten
267 amphibole-bearing peridotites. The $Fe^{3+}$ concentration of metasomatic $Grt_2$ from Sulu (yellow
268 squares) varies between 0.03 and 0.07 a.p.f.u., similar to most of the analysed garnets from
269 Maowu samples. Also, they show the similar negative correlation of $Fe^{3+}$ with Al, indicating
270 the reciprocal substitution in the octahedral site of garnet, sensitive to the redox condition of
271 the mineral. Garnets from the Ulten peridotite (empty circles) show the highest $Fe^{3+}$
272 concentrations, comparable with the most enriched ones of sample RPC171 from Maowu.
273 The Al-$Fe^{3+}$ correlation of garnets from Sulu peridotites is less steep with respect to the other
274 rock samples, likely due to their Cr-rich composition.
275
276 *4.1.2. $Fe^{3+}$ in mineral infillings of multiphase inclusions*

277 Multiphase inclusions trapped by $Grt_2$ of Maowu orthopyroxenites have negative
278 crystal shapes and constant volume proportions of the mineral infillings (Fig. 3A). They
279 mainly consist of spinel, ± orthopyroxene and hydrous phases (gedrite/pargasite, chlorite,
280 phlogopite, ±talc, ±apatite). For petrographic, geochemical and crystallographic details see
281 Malaspina et al. (2006, 2009, 2015). As reported in Table 1, spinel is $Al_2O_3$-rich and may
282 contain up to 5.63 wt.% of ZnO. Differently as one would expect, this phase is the one with
283 the lowest $Fe_2O_3$ concentration with respect to the other mineral phases in the inclusions (Tab.
284 1 and Fig. 4). The mineral with the highest $Fe^{3+}/\Sigma Fe$ is in fact chlorite (up to 0.69), almost
285 corresponding to clinochlore, followed by phlogopite (0.26 to 0.70), gedrite (0.35 to 0.49),
286 pargasite (0.07) and Mg-hornblende amphibole (0.09).
287 In order to correlate the $Fe^{3+}$ distribution among the minerals filling the multiphase
288 inclusions, we plotted in Figure 6 the equilibrium assemblage of single inclusions in a
289 chemographic representation for the system $Fe_3O_4$–FeO–$CaMg_{0.5}AlSi_{1.5}O_6$–$KAlSiO_4$ at fixed
290 $SiO_2$ chemical potential, projected through the $FeMg_{-1}$ exchange vector. Each volume
291 corresponds to a single inclusion composed by spinel, phlogopite, chlorite and amphiboles.
292 The diagram of Figure 6 therefore plots both the relative positions of the single phases
293 composing the inclusions, indicating the partitioning of $Fe^{3+}$ between spinel, chlorite,
294 phlogopite and amphiboles, and the whole phase assemblage fields, which intersect each
295 other. This indicates that although the single phases record a different relative enrichment in
296 $Fe_3O_4$ component (representing the $Fe^{3+}$ atoms per formula units: e.g. $Fe^{3+}$ partitions in
297 chlorite and phlogopite with respect to spinel and Mg-hornblende), the whole oxygen budget
298 (i.e., the number of moles of the oxygen component, $nO_2$) of the inclusions is almost the same
299 and corresponds to the intersection field between the volumes.
300
301 **4.2. Liquid water in multiphase solid inclusions and micro-Raman results**

Liquid water preserved in some multiphase inclusions has been detected and mapped by high resolution FTIR-FPA imaging. Figures 7A and B show the imaging results on a multiphase inclusion of ~40×50 μm and three selected absorption spectra relative to the inclusion portions defined by blue, green and yellow-to-red colours. The fundamental absorptions of the molecule $H_2O$ are bands at 3400 $cm^{-1}$ (symmetric at 3220 $cm^{-1}$ and antisymmetric at 3445 $cm^{-1}$ stretching modes) and 1630 $cm^{-1}$ (bending mode) wavenumbers (Aines and Rossman, 1984). Since the two stretching modes of $H_2O$ near 3400 wavenumbers likely overlap the M-OH stretching of some hydrous minerals, such as chlorite (see later), the bending mode near 1630 $cm^{-1}$ has been selected as evidence of not bonded molecules of liquid $H_2O$ (Aines and Rossman, 1984). This assumption is justified by the fact that IR spectra of clinochlore in the region between 1700 and 1500 $cm^{-1}$ do not record any band (Schroeder, 2000), while it shows a characteristic band in the 3400-3600 $cm^{-1}$ region (Prieto et al., 1991). A study on Fe-rich clinochlore at room temperature by Gopal et al. (2004) assign the band at 1627 $cm^{-1}$ of their IR spectrum to "absorbed water-OH stretching", indicating "a strong coordination of the metal ion with the surrounding –OH groups".

In order to better understand the actual distribution of $H_2O$ with respect to the whole multiphase inclusion, we collected an X-ray micro-tomography 3D image (Fig. 7C). The brightness in the three images is an inverse function of X-ray absorption, where bright portions show regions of low absorption (low-density phases), and dark portions show regions of high absorption (high-density phases) from three different points of view. The bright low-density region of the inclusion perfectly corresponds to the $H_2O$-rich region shown by FTIR-FPA imaging (red region in Fig. 7A) and suggests that the low-density phase fills a ring-shaped space between the host garnet and a higher density region (solid silicate) in the center of the inclusion.

Detailed micro-Raman spectroscopy (Fig. 8) reveals that orthopyroxene, chlorite and nano-sized crystals of amphibole coexist with $H_2O$ in the multiphase inclusion shown in Figure 7. Half of the inclusion volume is filled by enstatite, identified by its main Raman vibrations at 1013, 688, 668, and 346 $cm^{-1}$ (Frezzotti et al., 2012), and minor bands at 1036, 865 and 542 $cm^{-1}$ (Raman Spectra Database Lyon, http://www.ens-lyon.fr/LST/Raman). As shown in Figure 8, enstatite is over/inter-grown with micro- to nano-crystals of amphibole, whose Raman vibrations correspond to grunerite-cummingtonite series, a monoclinic form of Mg-Fe-Mn-Li amphiboles group (Leake et al., 1997). Note that an orthorhombic form of amphibole from the same group is gedrite, which is very common in multiphase inclusions from these orthopyroxenites (Malaspina et al., 2015). Mg-bearing grunerite has been mainly identified by its peculiar band distribution in the $OH^-$ region at 3675, 3662, 3645, 3625 $cm^{-1}$, as described by Leissner et al. (2015). A different band distribution at 3689, 3632 and 3445 $cm^{-1}$ identifies the $OH^-$ region of Mg-rich chlorite with a characteristic broad shape of the $OH^-$ stretching vibration (e.g. Prieto et al., 1991; Frezzotti et al., 2012) .

## 5. INTENSITY VERSUS EXTENSITY: OXYGEN FUGACITY AND REDOX BUDGET

The oxidation state of many rock systems (e.g. mafic and ultramafic) is described by oxygen fugacity ($fO_2$), an intensive variable usually calculated from inverse modelling of phase equilibria. The interpretation of oxygen fugacities should take into account the fact that the "fugacity" concept is just a conventional representation of the oxygen chemical potential ($\mu O_2$) and its variations at constant P and T are the result of varying proportions of all the constituent chemical components (Evans, 2006; Malaspina et al., 2009b; Evans, 2012). When we consider peridotitic rocks, although the value of $\mu O_2$ is constrained by olivine +

352 orthopyroxene + spinel/garnet assemblage (e.g. O'Neill and Wall, 1987; Luth et al., 1990;
353 Wood, 1991; Gudmundsson and Wood, 1995), the relationship between $\mu O_2$ and the phase
354 assemblages stabilised for example by metasomatic processes is entirely unknown. This is
355 due to the fact that we know very little about the correlation between the intensive variable
356 $\mu O_2$ (or $fO_2$), the number of moles of $O_2$ (namely net bulk oxidation or redox budget) and the
357 $Fe^{3+}$ partitioning between the mineral phases. In 1991 Frost pointed out that the intensive
358 variable $fO_2$ is by definition independent of the relative proportion of the phases in a rock,
359 whereas reactions such as those used to evaluate the oxidation state of an equilibrium phase
360 assemblage, should require an oxygen mass balance (Frost 1991; Frost and Ballhaus, 1998).
361 In this context, the role of solid solutions, expecially of non-ideal ones, is of primary
362 importance because the behaviour of $Fe^{3+}$ partitioning between garnet and pyroxenes, in a
363 mantle rock, could yield to misleading interpetations if $fO_2$ is calculated considering the $Fe^{3+}$
364 concentration of garnet (or spinel) only. We will clarify this point in section 5.2.

365 More complications arise if we consider that redox reactions depend on the
366 "abundance" of redox-sensitive elements and on the moles of oxygen exchanged in the redox
367 equilibria. Oxygen is in fact the most common electron acceptor in Earth systems and
368 oxidation and reduction generally mean gain and loss of oxygen (Evans 2006). However, in
369 the Earth's interior $O_2$ cannot be considered unequivocally a perfectly mobile component, as
370 defined by Korzhinskii (1959), because most of the redox reactions take place between solid
371 oxides and silicates, where oxygen is bonded to relatively inert components such as FeO (then
372 forming $Fe_2O_3$ and viceversa). On this principle, the amount of inert components has a
373 fundamental role and the molar quantity of exchanged $O_2$ should be considered as an
374 independent state variable. This means that the extensive variable $nO_2$ (moles of oxygen),
375 instead of $\mu O_2/fO_2$ should be considered for the redox budget determination of a rock system,
376 particularly when its bulk composition is modified by metasomatic chemical exchanges. In

these occurrences, molar quantities other than $nO_2$ are not constant, and the $\mu O_2$ conjugate chemical potential is not a simple increasing/decreasing function of the quantity of oxygen. Therefore, the reconstruction of the extensive redox budget of the rock from the intensive variable $fO_2$ can yield to a real paradox given by a decoupling between these two variables (Evans, 2006; Malaspina et al., 2009b). Nice natural examples of such decoupling are represented by the "ultra-oxidised" subduction mélanges Mn-eclogites from Italian Western Alps (Tumiati et al., 2015), hematite-bearing subducted serpentinites from the Cerro del Almirez massif in Spain (Debret et al., 2015), and sulfide-oxide-bearing eclogites from Tianshan in China (Li et al., 2016). These case studies all represent a geodynamic scenario of a mélange forming at the slab-mantle interface, pervasively infiltrated by fluids produced by dehydration reactions during subduction, where the $fO_2$ variations do not resemble the amount of $nO_2$ involved in the redox reactions.

In the next sections we will compare the oxygen fugacity of our orthopyroxenite samples with their bulk oxidation state, and evaluate the amount of oxygen provided by the slab-derived fluid phases (multiphase inclusions) during fluid/rock interactions likely occurring at the slab-mantle interface.

### 5.1. Oxygen fugacity of Maowu orthopyroxenite

We calculated the $fO_2$ of MWF2 and MWF2A garnet-orthopyroxenite samples by a forward modelling, starting from the redox equilibrium between the $Fe^{3+}$-garnet component skiagite, olivine and orthopyroxene (Gudmundsson and Wood, 1995; Woodland and Peltonen, 1999). Calculations were performed using the Gibbs free energy minimisation programme Vertex/Perple_X (http://www.perplex.ethz.ch; Connolly, 1990), integrating solid solution models for garnet (pyrope–grossular–almandine–skiagite; Malaspina et al., 2009b),

olivine (forsterite–fayalite; Holland and Powell, 1998) and orthopyroxene (enstatite–ferrosilite; Holland and Powell, 1996). The $fO_2$ is retrieved by selecting the redox equilibria where the pseudocomponents in garnet, olivine and orthopyroxene approach those of the investigated samples (Tab. 1). The resulting pseudo-univariant redox equilibria are shown in Figure 9 (dashed curves), which portrays an isobaric T-log$fO_2$ section computed at 4 GPa. The pseudocompounds selected are olivine with 90 mol% of forsterite ($Fo_{90}$), orthopyroxene with 93 mol% of enstatite ($En_{93}$), and garnet with 72 mol% of pyrope ($Py_{72}$), 4 mol% of grossular ($Gr_4$), and variable skiagite (Ski)–almandine (Alm) content as a function of the redox-sensitive $Fe^{3+}$–Al substitution in the octahedral site of garnet. The resulting equilibrium was chosen on the basis of the $Fe^{3+}$ content measured in garnet (Tab. 1), properly balanced following Malaspina and Tumiati (2012), and is expressed as follows:

$$1\ Py_{72}Gr_4Alm_{23}Ski_1 = 0.98\ Py_{69}Gr_5Alm_{24} + 0.03\ Fo_{90} + 0.015\ En_{93} + 0.015\ O_2 \quad (1)$$

As shown in Figure 9, the oxygen fugacities resulting from eq. (1) at the peak equilibration conditions of 4 GPa and 750-800 °C are: log$fO_2$ = -14.8 ÷ -13.5, which correspond to ΔFMQ = -1.8 ÷ -1.5, using the fayalite-magnetite-quartz oxygen buffer as reference (black solid line in Fig. 9). Being $fO_2$ an intensive variable, the reference to the equilibrium such as FMQ is necessary to compare the obtained results from eq. (1) with the oxygen fugacities of supra-subduction garnet peridotites from Sulu and Ulten, equilibrated at different P-T conditions. The balanced equilibrium reported by Malaspina and Tumiati (2012) and the resulting ΔFMQ from the Sulu peridotite is:

$$1\ Py_{67}Gr_{13}Alm_{16}Ski_4 = 0.96\ Py_{64}Gr_{14}Alm_{23} + 0.08\ Fo_{89} + 0.02\ En_{89} + 0.02\ O_2 \quad (2)$$

with $fO_2$ ranging bewteen FMQ and FMQ+1.5 at 5 GPa and 900 °C. Similar results (FMQ – FMQ+2, at 3 GPa and 850 °C) are recorded by the Ulten peridotites:

$$1\ Py_{65}Gr_{14}Alm_{18}Ski_3 = 0.97\ Py_{62}Gr_{14}Alm_{23} + 0.06\ Fo_{89} + 0.02\ En_{89} + 0.02\ O_2 \quad (3)$$

426 Comparing the resulting oxygen fugacities of Maowu orthopyroxenites with those of Sulu and
427 Ulten peridotites, the samples studied in this work look more reduced in terms of ΔFMQ.
428
429 **5.2. Bulk rock oxidation state and the role of $Fe^{3+}$ distribution between mineral phases**
430
431 The estimation of an oxygen mass balance is mandatory to evaluate the oxidation state
432 of an equilibrium phase assemblage, particularly when $fO_2$ of garnet-lherzolites is calculated
433 from equilibria where clinopyroxene is not involved, e.g. (Luth et al., 1990):
434 skiagite = 2 fayalite + ferrosilite + 0.5 $O_2$ (4)
435 and/or
436 andradite + pyrope + 2 ferrosilite = grossular + 2 fayalite + 3 enstatite + 0.5 $O_2$ (5)
437 Several studies demonstrated that the increase of $Fe^{3+}$ in garnet with increasing temperature is
438 not a simple relation with the whole rock $Fe_2O_3$, but is rather the consequence of the
439 partitioning of $Fe^{3+}$ from clinopyroxene into garnet (Canil and O'Neill, 1996; Woodland and
440 Peltonen, 1999; Woodland and Koch, 2003; Rohrbach et al., 2007; Woodland, 2009;
441 Rohrbach et al., 2011). Furthermore, clinopyroxene in metasomatised garnet peridotites may
442 enrich in $Fe^{3+}$ as aegerine component (Woodland, 2009) and potentially becomes the major
443 $Fe^{3+}$ host when peridotites are metasomatised by $Fe_2O_3$- and alkali-rich fluid phases
444 (Malaspina et al., 2012). Finally, also orthopyroxene may contain up to 10% of $Fe^{3+}$ with
445 respect to its total iron (Canil and O'Neill, 1996; Nimis and Grütter, 2010; Malaspina et al.,
446 2012; Nimis et al., 2015), indicating that the assumption of negligible $Fe^{3+}/\Sigma Fe$ values (<0.05)
447 in the activity correction of ferrosilite component (Gudmundsson and Wood, 1995) may result
448 in systematic errors of $fO_2$ conditions.
449 A useful approach to relate the $Fe^{3+}$ redistribution between mineral phases to the bulk
450 rock oxidation state, is plotting the compositions of equilibrium assemblages in barycentric

mole fractions. The Maowu orthopyroxenites studied here show very rare clinopyroxene and orthopyroxene does not contain $Fe^{3+}$ (Fig. 4). We therefore used the same chemographic representation portrayed in Figure 6, from a different perspective, to plot the MWF2A bulk rock composition, and compared it with the mulitphase inclusion mineral assemblages (likely the metasomatic fluid composition) together with reference lherzolite and harzburgite (Figure 10). The bulk rock major element composition is from Malaspina et al. (2006), while the FeO (=5.36 wt.%) and $Fe_2O_3$ (=0.92 wt.%) have been determined by chemical titration, dissolving 0.2 g of powdered samples in a hot mixture of 10 ml $H_2SO_4$ conc., 20 ml HF 50%, and 10 $H_2O$ in a PTFE becker. The solution obtained was then diluted and titrated with a 0.1 N solution of $KMnO_4$. With respect to a model mantle harzburgite and lherzolite (HZ-LZ), our metasomatic orthopyroxenite results more "oxidised", i.e. more enriched in bulk $nO_2$, being its composition similar in terms of kalsilite and Ca-Tschermak components, but enriched in terms of magnetite component. It is worthy of note that our sample plots between HZ and the grey and pink volumes given by the mineral compositions of the multiphase inclusions. This suggests that the interpretation that the composition of the Maowu orthopyroxenites may represent a hybrid rock resulting from a previous harzburgite fluxed by crust-derived metasomatic liquids is consistent also in terms of oxygen mass balance.

### 5.3. Redox budget of the multiphase inclusions

Even if an interaction between the fluid phase and the host garnet did occur (Malaspina et al., 2015), the inclusion system is locally a closed system, as evidenced by the fact that liquid water is still preserved in some multiphase inclusions (Fig. 7). In order to quantify the redox budget of multiphase inclusions and to compare it with other slab and supra-subduction mantle rocks, we need to evaluate the quantity of $nO_2$, which in turn

476 depends on the mineral abundances. A simple way to make the oxygen mass balance of a
477 mineral assemblage explicit is to consider key phases as components of the rock system as
478 shown in Figures 6 and 10, where the increase of $nO_2$ is indicated by the grey arrows pointing
479 to the magnetite apex. Alternatively, as shown by Tumiati et al. (2015), we can consider the
480 contribution of $Fe^{3+}$-bearing minerals by considering the $O_2$ not as a phase or species but as a
481 component. In the multiphase inclusions the relative proportions of each phase are not
482 accessible. We could therefore consider as lower limit for $nO_2$ per unit volume a cavity
483 composed by 100% of host garnet, and as upper limit a cavity filled by 100% of $Fe^{3+}$-chlorite
484 (i.e. the phase most enriched in $Fe_2O_3$, Fig. 4 and Tab. 1). One mole of host garnet
485 composition will be:

486 $$(MgO)_{2.13}(CaO)_{0.14}(FeO)_{0.74}(AlO_{1.5})_{1.93}(SiO_2)_{2.96}\ (O_2)_{0.008}$$

487 and one mole of $Fe^{3+}$-chlorite will be:

488 $$(MgO)_{9.06}(FeO)_{1.00}(AlO_{1.5})_{4.25}(SiO_2)_{5.64}(H_2O)_{0.63}\ (O_2)_{0.15}.$$

489 The moles of excess oxygen can be calculated considering the molar volume of garnet
490 or chlorite as a single phase in the inclusion. The resulting redox budget of the multiphase
491 inclusions therefore ranges from 0.05 to 0.4 mmol $cm^{-3}$. Based on mass balance calculation
492 considering the bulk rock composition as reported by Malaspina et al. (2006), integrated with
493 measured FeO-$Fe_2O_3$ wt.% (section 5.2), and the minerals chemistry (Tab. 1), the whole
494 orthopyroxenite results composed by 10 mol% of garnet and 90 mol% of orthopyroxene.
495 Considering the molar volume of these minerals, the rock composition contributes to 0.011
496 mmol $cm^{-3}$ of excess oxygen. This approach enables to make a comparison with other rock
497 systems in a geodynamic scenario for the slab-mantle interface as portrayed in Figure 11. A
498 mafic eclogite, simplified as bimineralic garnet + clinopyroxene rock with a 1:1 ratio, would
499 be characterised by 0.2 mmol $cm^{-3}$ of excess $O_2$ (clinopyroxene and garnet compositions from
500 Proyer et al., 2004). On the other hand, assuming 5 mol% of garnet and 5 mol% of

clinopyroxene (other than olivine and orthopyroxene) in a supra-subduction mantle peridotite, the excess $O_2$ would be characterised by 0.013 mmol $cm^{-3}$ (clinopyroxene and garnet compositions from Malaspina et al., 2012). As a consequence, because mass transfer is supported by chemical gradients, in this case by gradient in $nO_2$, a metasomatic front develops from the oxidised slab (red layer in Fig. 11) to the overlying mantle wedge (green layer in Fig. 10) passing through a transitional layer of hybrid rocks (dotted field in Fig. 10).

In geodynamic settings where a high fluid/rock ratio is expected, such as subduction mélange, oxygen is likely transported along fractures and veins, possibly through mechanisms of dissolution–reprecipitation of O-enriched oxides and silicates (Tumiati et al., 2015), or by advective processes (Marschall and Schumacher, 2012; Tumiati et al., 2013). On the other hand, fluid percolation at low fluid/rock ratios likely occurs when the metasomatic fluid phases leave the slab-mantle interface. Metasomatised supra-subduction peridotites show in fact evidence of percolation by aqueous fluids and/or supercritical liquids mainly by the occurrence of fluid inclusions (Song et al., 2009; Kawamoto et al., 2013) or multiphase solid inclusions (e.g. Van Roermund and Carswell, 2002; Malaspina et al., 2006; Scambelluri et al., 2008; Vrijmoed et al., 2008; Malaspina et al., 2010). $Fe^{3+}$ may become highly mobile in melt-like fluids at ultrahigh pressure (Hirschmann, 2009; Kelley and Cottrell, 2009). Supercritical liquids produced by the subducting slab could be therefore efficient oxygen carryers, providing some information of their redox budget if trapped as multiphase inclusions (yellow layer and little hexagons in Figure 10).

## 6. CONCLUSIONS

Information on fluid-mediated element transfer and redox processes occurring at the slab-mantle interface can be gained by the study of orogenic metasomatised ultramafic rocks

associated with deeply subducted crust such as the Maowu orthopyroxenites. Forward modelling $fO_2$ calculations indicate that the garnet orthopyroxenites are apparently more reduced with respect to metasomatised supra-subduction garnet-peridotites. On the other hand, oxygen mass balance, performed both on the Maowu hybrid orthopyroxenite and on metasomatised supra-subduction garnet peridotites, indicate that the excess of oxygen ($nO_2$) is the same and corresponds to 10 mol $m^{-3}$.

Slab-derived fluid phases are still preserved as primary multiphase solid inclusions in garnets. This is evidenced by the local occurrence of liquid water, precluding a leakage of fluid during decompression. To investigate the redox budget of these fluid phases, the $Fe^{3+}$ concentration of the micron-sized microprecipitates of the multiphase inclusions has been measured for the first time by TEM-EELS. Results indicate that the solute content of deep slab fluids may contain high $Fe^{3+}$ concentrations even after the interaction with the host garnet during the precipitation of the daughter phases. An oxygen mass balance also indicates that the fluid precipitates are more oxidised than the host rock (Fig. 10), reaching up to 400 mol $m^{-3}$ of $nO_2$. This suggests that even after their interaction with the metasomatic orthopyroxenites, the residual fluid phases could be potentially carrier of oxidised components when escaping the slab-mantle interface. This is shown in Figure 10 where the grey arrows trace an ideal path from a model harzburgite (HZ) and lherzolite (LZ) to the composition of $Fe^{3+}$-rich glasses from backarc (BABB) and melt inclusions (MI) from arc lavas. Such a trend crosses the compositional space of both the Maowu orthopyroxenite and the phase assemblage of the slab-derived residual fluid.

This gradient in $nO_2$ can be modelled as a metasomatic front developing from the oxidised slab to the overlying lithospheric mantle wedge passing through a transitional layer of hybrid rocks at the slab-mantle interface (Fig. 11).

## Acknowledgments

L. Chelazzi (University of Firenze) and S. Ferrando (University of Torino) are ackowledged for the analytical assistance in X-ray microCT and micro-Raman, respectively. V. Pasini and S. Santacesaria (SRA Instruments SpA) provided the access to the facility for imaging FTIR-FPA measurements and data processing. Discussion with D. Ami (University of Milano Bicocca) on FTIR spectra has been much appreciated. N. Malaspina, S. Tumiati and S. Poli thank the financial support by the Italian Ministry of Education, University and Research (MIUR) [PRIN-2012R33ECR]. This work also benefited from the University of Milano Bicocca FAR12/13 (12-1-2009100-139). F. Langenhorst thanks for financial support by the Leibniz program of the Deutsch Forschungsgemeinschaft (LA 830/14-1).

## References cited

Aines R. D. and Rossman G. R. (1984) Water in minerals? A peak in the infrared. *J. Geophys. Res.* **89**, 4059–4071.

van Aken P. A., Liebscher B. and Styrsa V. J. (1998) Quantitative determination of iron oxidation states in minerals using Fe L 2,3 -edge electron energy-loss near-edge structure spectroscopy. *Phys. Chem. Miner.* **25**, 323–327.

Ayers J. C., Dunkle S., Gao S. and Miller C. F. (2002) Constraints on timing of peak and retrograde metamorphism in the Dabie Shan Ultrahigh-Pressure Metamorphic Belt, east-central China, using U–Th–Pb dating of zircon and monazite. *Chem. Geol.* **186**, 315–331.

Brandon A. D. and Draper D. S. (1996) Constraints on the origin of the oxidation state of mantle overlying subduction zones: An example from Simcoe, Washington, USA. *Geochim. Cosmochim. Acta* **60**, 1739–1749.

Canil D. and O'Neill H. S. C. (1996) Distribution of Ferric Iron in some Upper-Mantle Assemblages. *J. Petrol.* **37**, 609–635.

Creighton S., Stachel T., Eichenberg D. and Luth R. W. (2009) Oxidation state of the lithospheric mantle beneath Diavik diamond mine, central Slave craton, NWT, Canada. *Contrib. to Mineral. Petrol.* **159**, 645–657.

Debret B., Bolfan-Casanova N., Padrón-Navarta J. A., Martin-Hernandez F., Andreani M., Garrido C. J., López Sánchez-Vizcaíno V., Gómez-Pugnaire M. T., Muñoz M. and Trcera N. (2015) Redox state of iron during high - pressure serpentinite dehydration. *Contrib. to Mineral. Petrol.* **169**.

Endo S., Mizukami T., Wallis S. R., Tamura A. and Arai S. (2015) Orthopyroxene-rich Rocks from the Sanbagawa Belt (SW Japan): Fluid–Rock Interaction in the Forearc Slab–Mantle Wedge Interface. *J. Petrol.* **56**, 1113–1137.

Evans K. A. (2006) Redox decoupling and redox budgets: Conceptual tools for the study of earth systems. *Geology* **34**, 489.

589 Evans K. A. (2012) The redox budget of subduction zones. *Earth-Science Rev.* **113**, 11–32.
590 Frezzotti M. L. and Ferrando S. (2015) The chemical behavior of fluids released during deep
591 subduction based on fluid inclusions. *Am. Mineral.* **100**, 352–377.
592 Frezzotti M. L., Tecce F. and Casagli A. (2012) Raman spectroscopy for fluid inclusion
593 analysis. *J. Geochemical Explor.* **112**, 1–20.
594 Frost B. R. and Ballhaus C. (1998) Comment on "Constraints on the origin of the oxidation
595 state of mantle overlying subduction zones: An example from Simcoe, Washington,
596 USA" *Geochim. Cosmochim. Acta* **62**, 329–331.
597 Frost D. J. and Langenhorst F. (2002) The effect of Al2O3 on Fe-Mg partitioning between
598 magnesiowustite and magnesium silicate perovskite. *Earth Planet. Sci. Lett.* **199**, 227–
599 241.
600 Frost D. J. and McCammon C. A. (2008) The Redox State of Earth's Mantle. *Annu. Rev.*
601 *Earth Planet. Sci.* **36**, 389–420.
602 Gopal N. O., Narasimhulu K. V. and Lakshmana Rao J. (2004) Optical absorption, EPR,
603 infrared and Raman spectral studies of clinochlore mineral. *J. Phys. Chem. Solids* **65**,
604 1887–1893.
605 Green D. H. (1963) Alumina content of enstatite in a Venezuelan high-temperature peridotite.
606 *Geol. Soc. Am. Bull.* **74**, 1397–1402.
607 Hanger B. J., Yaxley G. M., Berry A. J. and Kamenetsky V. S. (2015) Relationships between
608 oxygen fugacity and metasomatism in the Kaapvaal subcratonic mantle, represented by
609 garnet peridotite xenoliths in the Wesselton kimberlite, South Africa. *Lithos* **212–215**,
610 443–452.
611 Hirschmann M. M. (2009) Ironing Out the Oxidation of Earth' s Mantle. *Science* **325**, 545–
612 546.
613 Hofer H. E. and Brey G. P. (2007) The iron oxidation state of garnet by electron microprobe:
614 Its determination with the flank method combined with major-element analysis. *Am.*
615 *Mineral.* **92**, 873–885.
616 Jahn B., Fan Q., Yang J.-J. and Henin O. (2003) Petrogenesis of the Maowu pyroxenite–
617 eclogite body from the UHP metamorphic terrane of Dabieshan: chemical and isotopic
618 constraints. *Lithos* **70**, 243–267.
619 Kawamoto T., Yoshikawa M., Kumagai Y., Mirabueno M. H. T., Okuno M. and Kobayashi
620 T. (2013) Mantle wedge infiltrated with saline fluids from dehydration and
621 decarbonation of subducting slab. *Proc. Natl. Acad. Sci. U. S. A.* **110**, 9663–8.
622 Kelley K. A. and Cottrell E. (2009) Water and the oxidation state of subduction zone
623 magmas. *Science* **325**, 605–7.
624 Kessel R., Schmidt M. W., Ulmer P. and Pettke T. (2005) Trace element signature of
625 subduction-zone fluids, melts and supercritical liquids at 120-180 km depth. *Nature* **437**,
626 724–7.
627 Leake B. E., Woolley A. R., Arps C. E. S., Birch W. D., Gilbert C. M., Grice J. D.,
628 Hawthorne F. C., Kato A., Kisch H. J., Krivovichev V. G., Linthout K., Laird J.,
629 Mandarino J. A., Maresch W. V., Nickel E. H., Rock N. M. S., Schumacher J. C., Smith
630 D. C., Stephenson N. C. N., Ungaretti L., Whittaker E. J. W. and Youzhi G. (1997)
631 Nomenclature of amphiboles: report of the subcommittee of the international
632 commission, commission on new minerals and mineral names. *Can. Mineral.* **35**, 219–
633 246.
634 Leissner L., Schlüter J., Horn I. and Mihailova B. (2015) Exploring the potential of Raman
635 spectroscopy for crystallochemical analyses of complex hydrous silicates: I.
636 Amphiboles. *Am. Mineral.* **100**, 2682–2694.
637 Li J.-L., Gao J., Klemd R., John T. and Wang X.-S. (2016) Redox processes in subducting
638 oceanic crust recorded by sulfide-bearing high-pressure rocks and veins (SW Tianshan,

China). *Contrib. to Mineral. Petrol.* **171**, 72.
Liou J. G. and Zhang R. Y. (1998) Petrogenesis of an ultrahigh-pressure garnet-bearing ultramafic body from Maowu, Dabie Mountains, east-central China. *Isl. Arc* **7**, 115–134.
Malaspina N., Alvaro M., Campione M., Wilhelm H. and Nestola F. (2015) Dynamics of mineral crystallization from precipitated slab-derived fluid phase: first in situ synchrotron X-ray measurements. *Contrib. to Mineral. Petrol.* **169**.
Malaspina N., Hermann J. and Scambelluri M. (2009a) Fluid/mineral interaction in UHP garnet peridotite. *Lithos* **107**, 38–52.
Malaspina N., Hermann J., Scambelluri M. and Compagnoni R. (2006) Polyphase inclusions in garnet–orthopyroxenite (Dabie Shan, China) as monitors for metasomatism and fluid-related trace element transfer in subduction zone peridotite. *Earth Planet. Sci. Lett.* **249**, 173–187.
Malaspina N., Langenhorst F., Fumagalli P., Tumiati S. and Poli S. (2012) Fe3+ distribution between garnet and pyroxenes in mantle wedge carbonate-bearing garnet peridotites (Sulu, China) and implications for their oxidation state. *Lithos* **146–147**, 11–17.
Malaspina N., Poli S. and Fumagalli P. (2009b) The oxidation state of metasomatized mantle wedge: Insights from C-O-H-bearing garnet peridotite. *J. Petrol.* **50**, 1533–1552.
Malaspina N., Scambelluri M., Poli S., Van Roermund H. L. M. and Langenhorst F. (2010) The oxidation state of mantle wedge majoritic garnet websterites metasomatised by C-bearing subduction fluids. *Earth Planet. Sci. Lett.* **298**, 417–426.
Malaspina N. and Tumiati S. (2012) The role of C-O-H and oxygen fugacity in subduction-zone garnet peridotites. *Eur. J. Mineral.* **24**, 607–618.
Marschall H. R. and Schumacher J. C. (2012) Arc magmas sourced from mélange diapirs in subduction zones. *Nat. Geosci.* **5**, 862–867.
McCammon C., Frost D., Smyth J., Laustsen H. M., Kawamoto T., Ross N. and van Aken P. (2004) Oxidation state of iron in hydrous mantle phases: implications for subduction and mantle oxygen fugacity. *Phys. Earth Planet. Inter.* **143–144**, 157–169.
Niida K. and Green D. H. (1999) Stability and chemical composition of pargasitic amphibole in MORB pyrolite under upper mantle conditions. *Contrib. to Mineral. Petrol.* **135**, 18–40.
Nimis P., Goncharov A., Ionov D. A. and McCammon C. (2015) Fe3+ partitioning systematics between orthopyroxene and garnet in mantle peridotite xenoliths and implications for thermobarometry of oxidized and reduced mantle rocks. *Contrib. to Mineral. Petrol.* **169**.
Nimis P. and Grütter H. (2010) Internally consistent geothermometers for garnet peridotites and pyroxenites. *Contrib. to Mineral. Petrol.* **159**, 411–427.
Prieto A. C., Dubessy J. and Cathelineau M. (1991) Structure-composition relationships in trioctahedral chlorites: A vibrational spectroscopy study. *Clays Clay Miner.* **39**, 531–539.
Rohrbach A., Ballhaus C., Golla-Schindler U., Ulmer P., Kamenetsky V. S. and Kuzmin D. V (2007) Metal saturation in the upper mantle. *Nature* **449**, 456–8.
Rohrbach a., Ballhaus C., Ulmer P., Golla-Schindler U. and Schonbohm D. (2011) Experimental Evidence for a Reduced Metal-saturated Upper Mantle. *J. Petrol.* **52**, 717–731.
Scambelluri M., Hermann J., Morten L. and Rampone E. (2006) Melt- versus fluid-induced metasomatism in spinel to garnet wedge peridotites (Ulten Zone, Eastern Italian Alps): clues from trace element and Li abundances. *Contrib. to Mineral. Petrol.* **151**, 372–394.
Scambelluri M., Pettke T. and van Roermund H. L. M. (2008) Majoritic garnets monitor deep subduction fluid flow and mantle dynamics. *Geology* **36**, 59.
Simakov S. K. (1998) Redox state of Earth' s upper mantle peridotites under the ancient

cratons and its connection with diamond genesis. *Geochim. Cosmochim. Acta* **62**, 1811–1820.

Song S., Su L., Niu Y., Lai Y. and Zhang L. (2009) CH4 inclusions in orogenic harzburgite: Evidence for reduced slab fluids and implication for redox melting in mantle wedge. *Geochim. Cosmochim. Acta* **73**, 1737–1754.

Tsay A., Zajacz Z. and Sanchez-Valle C. (2014) Efficient mobilization and fractionation of rare-earth elements by aqueous fluids upon slab dehydration. *Earth Planet. Sci. Lett.* **398**, 101–112.

Tumiati S., Fumagalli P., Tiraboschi C. and Poli S. (2013) An experimental study on COH-bearing peridotite up to 3.2 GPa and implications for crust-mantle recycling. *J Petrol* **54**, 453–479.

Tumiati S., Godard G., Martin S., Klötzli U. and Monticelli D. (2007) Fluid-controlled crustal metasomatism within a high-pressure subducted mélange (Mt. Hochwart, Eastern Italian Alps). *Lithos* **94**, 148–167.

Tumiati S., Godard G., Martin S., Malaspina N. and Poli S. (2015) Ultra-oxidized rocks in subduction mélanges? Decoupling between oxygen fugacity and oxygen availability in a Mn-rich metasomatic environment. *Lithos* **226**, 116–130.

Tumiati S., Thöni M., Nimis P., Martin S. and Mair V. (2003) Mantle–crust interactions during Variscan subduction in the Eastern Alps (Nonsberg–Ulten zone): geochronology and new petrological constraints. *Earth Planet. Sci. Lett.* **210**, 509–526.

Van Roermund H. M. L., Carswell D. A., Drury M. R. and Heijboer T. C. (2002) Microdiamonds in a megacrystic garnet websterite pod from Bardane on the island of Fjørtoft, western Norway: evidence for diamond formation in mantle rocks during deep continental subduction. *Geology* **30**, 959–962.

Vrijmoed J. C., Van Roermund H. L. M. and Davies G. R. (2006) Evidence for diamond-grade ultra-high pressure metamorphism and fluid interaction in the Svartberget Fe–Ti garnet peridotite–websterite body, Western Gneiss Region, Norway. *Mineral. Petrol.* **88**, 381–405.

Vrijmoed J., Smith D. and Roermund H. Van (2008) Raman confirmation of microdiamond in the Svartberget Fe–Ti type garnet peridotite, Western Gneiss Region, Western Norway. *Terra Nov.* **20**, 295–301.

Wang C., Liang Y., Dygert N. and Xu W. (2016) Formation of othopyroxenite by reaction between peridotite and hydrous basaltic melt: an experimental study. *Contrib. to Mineral. Petrol.* **171**, 1–18.

Wood B. J., Bryndzia L. T. and Johnson K. E. (1990) Tectonic Oxidation and Its Relationship to Tectonic Environment and Fluid Speciation. *Science (80-. ).* **248**, 337–345.

Woodland A. B. (2009) Ferric iron contents of clinopyroxene from cratonic mantle and partitioning behaviour with garnet. *Lithos* **112**, 1143–1149.

Woodland A. B. and Koch M. (2003) Variation in oxygen fugacity with depth in the upper mantle beneath the Kaapvaal craton, Southern Africa. *Earth Planet. Sci. Lett.* **214**, 295–310.

Woodland A. B., Kornprobst J. and Tabit A. (2006) Ferric iron in orogenic lherzolite massifs and controls of oxygen fugacity in the upper mantle. *Lithos* **89**, 222–241.

Xue F., Rowley D. B. and Baker J. (1996) Refolded syn-ultrahigh-pressure thrust sheets in the south Dabie complex, China: Field evidence and tectonic implications. *Geology* **24**, 455–458.

Yaxley G. M., Berry A. J., Kamenetsky V. S., Woodland A. B. and Golovin A. V. (2012) An oxygen fugacity profile through the Siberian Craton — Fe K-edge XANES determinations of Fe3+/∑Fe in garnets in peridotite xenoliths from the Udachnaya East kimberlite. *Lithos* **140–141**, 142–151.

Zhang R. Y., Liou J. G. and Cong B. L. (1995) Talc-, Magnesite- and Ti-Clinohumite-Bearing Ultrahigh-Pressure Meta-Mafic and Ultramafic Complex in the Dabie Mountains, China. *J. Petrol.* **36**, 1011–1037.

Zhang R. Y., Liou J. G., Yang J. S. and Yui T.-F. (2000) Petrochemical constraints for dual origin of garnet peridotites from the Dabie-Sulu UHP terrane , eastern-central China. *J. Metamorph. Geol.* **18**, 149–166.

**Figure captions**

Fig. 1

Cartoon representing the possible scenario occurring when slab-derived metasomatic agents (silica-saturated supercritical fluids, SCF, or melts) interact with peridotitic rocks at the slab-mantle interface. Modified after Scambelluri et al. (2006).

Fig. 2

Primitive mantle normalised trace element signature of multiphase inclusions in garnets of Maowu websterite and orthopyroxenite (pink area), compared with the trace element concentration of metasomatic clinopyroxene ($Cpx_2$) and phlogopite ($Phl_2$) from the Sulu garnet peridotite and of bulk rock metasomatised mantle peridotites from the Ulten Zone. Data from Malaspina et al. (2009a) and Scambelluri et al. (2006).

Fig. 3

A) Plane-polarised transmitted light image of multiphase solid inclusions (M. Inc.) in garnet core; B) bright-field TEM image of mineral infillings after ion milling preparation; C) high resolution TEM image of defect-free amphibole; inset shows the corresponding selected area electron diffraction pattern taken along the [-101] axis.

Fig. 4

767 Representative spectra of Fe $L_{32}$ electron energy-loss near-edge structure (ELNES) of mineral
768 phases crystallised in three different multiphase inclusions of the Maowu orthopyroxenite.
769 The spectra have been normalised to their maximum intensity and shifted vertically for
770 comparison.
771
772 Fig. 5
773 Negative correlation between Al and $Fe^{3+}$ (atoms per formula unit) measured in garnets from
774 the Maowu websterite (RPC171) and orthopyroxenites (MWF2 and MWF2A). Analyses of
775 the two garnet generations from the Sulu peridotite RPC684 (only cores) and of garnets from
776 metasomatised amphibole-bearing peridotites from Ulten Zone are also plotted for
777 comparison. Symbols refer to individual point analyses on single mineral grains for each
778 sample. Sulu and Ulten garnet analyses are the complete dataset from Malaspina et al.
779 (2009b).
780
781 Fig. 6
782 Chemographic representation for the system $Fe_3O_4$–FeO–$CaMg_{0.5}AlSi_{1.5}O_6$–$KAlSiO_4$ at fixed
783 $SiO_2$ chemical potential, projected through the $FeMg_{-1}$ exchange vector, showing the
784 multiphase solid inclusions mineral assemblages. For clarity, the scale of the FeO, $Fe_3O_4$ and
785 $KAlSiO_4$ corners has been magnified (2 FeO, 1/20 magnetite, 2 kalsilite).
786
787 Fig. 7
788 A) Plane polarised optical microscope image of a primary multiphase inclusion in garnet and
789 FTIR-FPA imaging of the $H_2O$ distribution at the characteristic 1630 $cm^{-1}$ wavenumber
790 absorption band (corresponding to the bending mode of the $H_2O$ molecule). Colours of the
791 imaging refer to the magnitude of such band, as reported in (B). B) Selected infrared

792 absorption spectra of the inclusion portions in (A), relative to the intensity of the 1630 $cm^{-1}$
793 bending mode of $H_2O$. The spectra also show the stretching modes of $H_2O$ near 3400 $cm^{-1}$
794 wavenumbers, overlapping the $Fe^{3+}$-OH stretching of chlorite. The high intensity band
795 between 1900 and 1700 $cm^{-1}$ wavenumber likely corresponds to the O-Si bond of silicates.
796 Abbreviations: PDC91=Prieto et al., 1991; GNR04=Gopal et al., 2004; A&R84=Aines and
797 Rossman, 1984. C) Different views of a 3D volume rendering from high-resolution microCT
798 slices acquired on multiphase inclusion of (A) and (B). In these images, the brightness is an
799 inverse function of X-ray absorption, with bright spots showing regions of low absorption,
800 and dark spots showing regions of high absorption.
801
802 Fig. 8
803 Representative Raman spectra of minerals coexistent with liquid $H_2O$ within the same
804 multiphase inclusion shown in Figure 7. For amphibole Mg-grunerite and chlorite the O-H
805 stretching modes in the range between 3000 and 4000 $cm^{-1}$ wavenumber are also reported.
806 Spectra are baseline corrected.
807
808 Fig. 9
809 Pseudo-univariant equilibria calculated at 4 GPa as a function of oxygen fugacity ($\log fO_2$) and
810 temperature. The dashed curves are the isopleths of Fe-Mg-Ca garnet solid solution with 72
811 mol% of pyrope, 4 mol% of grossular ($Py_{72}Gr_4$) and variable mol% of almandine and skiagite
812 as a function of $fO_2$, as defined by equilibrium (1). Invariant points refer to the change in
813 olivine composition to $Fo_{93}$. Fayalite-magnetite-quartz buffer (fa = q mt) is also plotted for
814 comparison.
815
816 Fig. 10

Different perspective of the chemographic representation of Figure 6, showing the bulk rock composition of the Maowu orthopyroxenite (red star) and the multiphase inclusions mineral assemblages (grey and pink volumes). The grey arrow traces an ideal path from a model harzburgite (HZ) and lherzolite (LZ) composition (Green, 1963; Niida and Green, 1999) to the composition of glasses from backarc (BABB) and melt inclusions (MI) from arc lavas (Katherine A. Kelley and Cottrell, 2009). The composition of a Mid Ocean Ridge glass (MORB) from the Mid Atlantic Ridge is also plotted for comparison (Katherine A. Kelley and Cottrell, 2009).

Fig. 11

Schematic cartoon showing the gradient of $nO_2$, corresponding to the quantity of oxygen in excess with respect to $Fe^{3+}$-free systems, from the subducted slab to the overlying mantle, through the slab-mantle interface. The coloured bar qualitatively indicates low and high "oxidised" regions for 1 $m^3$ of rock. Yellow exagons represent the multiphase inclusions in garnet orthopyroxenites. SCF = supercritical fluid phases. Redrawn after Tumiati et al. (2015).

Table 1

Average major element compositions (oxide wt.%), recalculated structural formulae and $Fe^{3+}/\Sigma Fe$ of garnets from Maowu websterite (RPC171) and orthopyroxenites (MWF2 – MWF2A), and from Sulu peridotite (RPC684). Numbers in square brackets are the number of analyses and numbers in brackets are the standard deviations of the averages. Compositions of representative orthopyroxenes and EDX analyses of multiphase inclusions mineral infillings from Maowu websterite and orthopyroxenite samples are also reported. Abbreviations: Grt,

841 garnet; py, pyrope; alm, almandine; gro, grossular; ski, skiagite; Opx, orthopyroxene; Amph,

842 amphibole; Chl, chlorite; Phl, phlogopite; Spl, spinel; INC, inclusion. *=iron as total FeO

# Table

Table 1

| Sample/inclusion | RPC171 | MWF2 | MWF2A | RPC684 | RPC684 | RPC171 | MWF2A | INC 1 (Host Garnet $Fe^{3+}/\Sigma Fe=0.11$) | | | | INC 2 (Host Garnet $Fe^{3+}/\Sigma Fe=0.11$) | | | | INC 3 (Host Garnet $Fe^{3+}/\Sigma Fe=0.11$) | | |
|---|---|---|---|---|---|---|---|---|---|---|---|---|---|---|---|---|---|---|
| Phase | Grt [19] | Grt [5] | Grt [7] | Grt 1 [4] | Grt 2 [11] | Opx | Opx | Amph (Mg-hbl) | Chl | Phl | Spl | Amph (Ged) | Amph (Prg) | Phl | Spl | Amph (Ged) | Amph (Ged) | Chl |
| $SiO_2$ | 41.16 (0.33) | 41.17 (0.22) | 41.55 (0.25) | 42.74 (0.18) | 42.14 (0.25) | 58.46 | 58.75 | 48.82 | 30.16 | 45.40 | n.a. | 42.94 | 40.92 | 45.40 | n.a. | 42.04 | 43.51 | 32.09 |
| $TiO_2$ | 0.02 (0.01) | 0.03 (0.00) | 0.02 (0.01) | 0.01 (0.01) | 0.02 (0.01) | 0.01 | 0.01 | n.a. | n.a. | n.a. | n.a. | n.a. | n.a. | n.a. | n.a. | n.a. | n.a. | n.a. |
| $Al_2O_3$ | 22.27 (0.36) | 22.99 (0.23) | 22.94 (0.39) | 23.22 (0.05) | 22.01 (0.75) | 0.08 | bdl | 13.36 | 19.27 | 14.36 | 65.43 | 21.26 | 19.48 | 14.36 | 64.15 | 21.71 | 19.01 | 17.48 |
| $Cr_2O_3$ | 0.58 (0.19) | 1.46 (0.20) | 1.64 (0.53) | 2.31 (0.03) | 2.77 (0.81) | 0.01 | 0.03 | 0.23 | n.a. | n.a. | 0.42 | 0.03 | n.a. | n.a. | 0.44 | n.a. | n.a. | n.a. |
| FeO | 12.24 (0.51) | 11.51 (0.36) | 11.60 (0.28) | 8.51 (0.34) | 9.73 (0.32) | *6.28 | 4.75 | 3.59 | 2.61 | 1.98 | 19.40 | 2.96 | 2.19 | 2.48 | 19.48 | 3.85 | 3.78 | 1.26 |
| $Fe_2O_3$ | 0.96 (0.27) | 0.62 (0.56) | 0.65 (0.39) | 0.57 (0.37) | 0.82 (0.24) | n.a. | 0.00 | 0.39 | 4.17 | 1.53 | 0.44 | 3.16 | 0.18 | 0.97 | 2.95 | 2.31 | 2.26 | 2.99 |
| MgO | 17.18 (0.37) | 20.15 (0.16) | 20.04 (0.37) | 19.46 (0.26) | 18.58 (0.13) | 36.18 | 37.48 | 15.39 | 32.53 | 26.66 | 10.30 | 22.93 | 23.64 | 26.66 | 7.20 | 24.62 | 24.08 | 34.79 |
| MnO | 0.46 (0.02) | 0.38 (0.01) | 0.40 (0.02) | 0.41 (0.03) | 0.62 (0.07) | 0.05 | 0.10 | n.a. | n.a. | n.a. | 0.45 | n.a. | n.a. | n.a. | 0.68 | n.a. | n.a. | n.a. |
| CaO | 4.37 (0.41) | 1.95 (0.11) | 1.78 (0.44) | 4.87 (0.02) | 4.53 (0.21) | 0.08 | 0.08 | 14.69 | n.a. | n.a. | 0.11 | 0.24 | 0.08 | n.a. | 0.11 | 0.56 | 0.31 | n.a. |
| $Na_2O$ | bdl | bdl | bdl | bdl | bdl | bdl | bdl | 1.11 | n.a. | n.a. | n.a. | 2.88 | 6.40 | n.a. | n.a. | 1.33 | 3.05 | n.a. |
| $K_2O$ | bdl | bdl | bdl | bdl | bdl | bdl | bdl | n.a. | n.a. | 7.90 | n.a. | n.a. | 0.96 | 7.90 | n.a. | 0.07 | 0.00 | n.a. |
| ZnO | n.a. | n.a. | n.a. | n.a. | n.a. | n.a. | n.a. | n.a. | n.a. | n.a. | 3.78 | n.a. | n.a. | n.a. | 5.63 | n.a. | n.a. | n.a. |
| Sum | 99.26 (1.02) | 100.26 (0.23) | 100.62 (0.35) | 102.09 (0.12) | 101.21 (0.57) | 101.16 | 101.20 | 97.57 | 88.75 | 97.83 | 100.34 | 96.39 | 93.87 | 97.77 | 100.64 | 96.50 | 95.99 | 88.60 |
| Si | 3.00 (0.01) | 2.95 (0.01) | 2.96 (0.01) | 2.99 (0.01) | 3.00 (0.02) | 1.99 | 1.99 | 6.82 | 5.64 | 6.08 | n.a. | 5.92 | 5.87 | 6.09 | n.a. | 5.79 | 6.05 | 5.94 |
| Ti | 0.00 (0.00) | 0.00 (0.00) | 0.00 (0.00) | 0.00 (0.00) | 0.00 (0.00) | 0.00 | 0.00 | n.a. | n.a. | n.a. | n.a. | n.a. | n.a. | n.a. | n.a. | n.a. | n.a. | n.a. |
| Al | 1.92 (0.02) | 1.94 (0.02) | 1.93 (0.03) | 1.91 (0.01) | 1.85 (0.06) | 0.00 | bdl | 2.20 | 4.25 | 2.27 | 2.04 | 3.46 | 3.29 | 2.27 | 2.03 | 3.53 | 3.11 | 3.81 |
| Cr | 0.03 (0.01) | 0.08 (0.01) | 0.09 (0.03) | 0.13 (0.00) | 0.16 (0.05) | 0.00 | 0.00 | 0.03 | n.a. | n.a. | 0.01 | 0.00 | 0.00 | n.a. | 0.01 | n.a. | n.a. | n.a. |
| $Fe^{2+}$ | 0.75 (0.03) | 0.69 (0.02) | 0.69 (0.02) | 0.50 (0.02) | 0.58 (0.02) | *0.18 | 0.13 | 0.42 | 0.41 | 0.22 | 0.43 | 0.34 | 0.26 | 0.28 | 0.44 | 0.44 | 0.44 | 0.20 |
| $Fe^{3+}$ | 0.05 (0.02) | 0.03 (0.03) | 0.03 (0.02) | 0.03 (0.02) | 0.04 (0.01) | n.a. | 0.00 | 0.04 | 0.59 | 0.15 | 0.01 | 0.33 | 0.02 | 0.10 | 0.06 | 0.24 | 0.24 | 0.42 |
| Mg | 1.87 (0.04) | 2.15 (0.01) | 2.13 (0.04) | 2.03 (0.02) | 1.97 (0.02) | 1.83 | 1.89 | 3.20 | 9.06 | 5.32 | 0.41 | 4.71 | 5.05 | 5.33 | 0.29 | 5.06 | 4.99 | 9.59 |
| Mn | 0.03 (0.00) | 0.02 (0.00) | 0.02 (0.00) | 0.02 (0.00) | 0.04 (0.00) | 0.00 | 0.00 | n.a. | n.a. | n.a. | 0.01 | n.a. | n.a. | n.a. | 0.02 | n.a. | n.a. | n.a. |
| Ca | 0.34 (0.03) | 0.15 (0.01) | 0.14 (0.03) | 0.36 (0.00) | 0.35 (0.02) | 0.00 | 0.00 | 2.20 | n.a. | n.a. | 0.00 | 0.04 | 0.01 | n.a. | 0.00 | 0.08 | 0.05 | n.a. |
| Na | bdl | bdl | bdl | bdl | bdl | bdl | bdl | 0.30 | n.a. | n.a. | n.a. | 0.77 | 1.78 | n.a. | n.a. | 0.36 | 0.82 | n.a. |
| K | bdl | bdl | bdl | bdl | bdl | bdl | bdl | n.a. | n.a. | 1.35 | n.a. | n.a. | 0.18 | 1.35 | n.a. | 0.01 | 0.00 | n.a. |
| Zn | n.a. | n.a. | n.a. | n.a. | n.a. | n.a. | n.a. | n.a. | n.a. | n.a. | 0.07 | n.a. | n.a. | n.a. | 0.11 | n.a. | n.a. | n.a. |
| Cations sum | 7.99 (0.01) | 8.02 (0.00) | 8.01 (0.01) | 7.98 (0.01) | 7.98 (0.01) | 4.01 | 4.01 | 15.20 | 19.94 | 15.39 | 2.97 | 15.57 | 16.46 | 15.41 | 2.95 | 15.51 | 15.69 | 19.95 |
| Charges sum | 24.00 | 24.00 | 24.00 | 24.00 | 24.00 | 12.00 | 12.00 | 46.00 | 56.00 | 44.00 | 8.00 | 46.00 | 46.00 | 44.00 | 8.00 | 46.00 | 46.00 | 56.00 |
| $Fe^{3+}/\Sigma Fe$ | 0.07 (0.02) | 0.05 (0.04) | 0.05 (0.03) | 0.06 (0.04) | 0.07 (0.02) | n.a. | 0.00 | 0.09 | 0.59 | 0.41 | 0.02 | 0.49 | 0.07 | 0.26 | 0.12 | 0.49 | 0.35 | 0.68 |
| py (mol%) | 62.48 (1.40) | 71.41 (0.30) | 71.46 (1.17) | 69.64 (0.63) | 67.36 (0.69) | | | | | | | | | | | | | |
| alm (mol%) | 24.59 (0.94) | 22.66 (0.90) | 22.98 (0.64) | 16.95 (0.76) | 19.55 (0.61) | | | | | | | | | | | | | |
| gro (mol%) | 11.42 (1.05) | 4.97 (0.30) | 4.56 (1.13) | 12.52 (0.10) | 11.80 (0.47) | | | | | | | | | | | | | |
| ski (mol%) | 1.51 (0.44) | 0.96 (0.86) | 1.00 (0.61) | 0.89 (0.57) | 1.29 (0.39) | | | | | | | | | | | | | |

**Figure 1**

Click here to download high resolution image

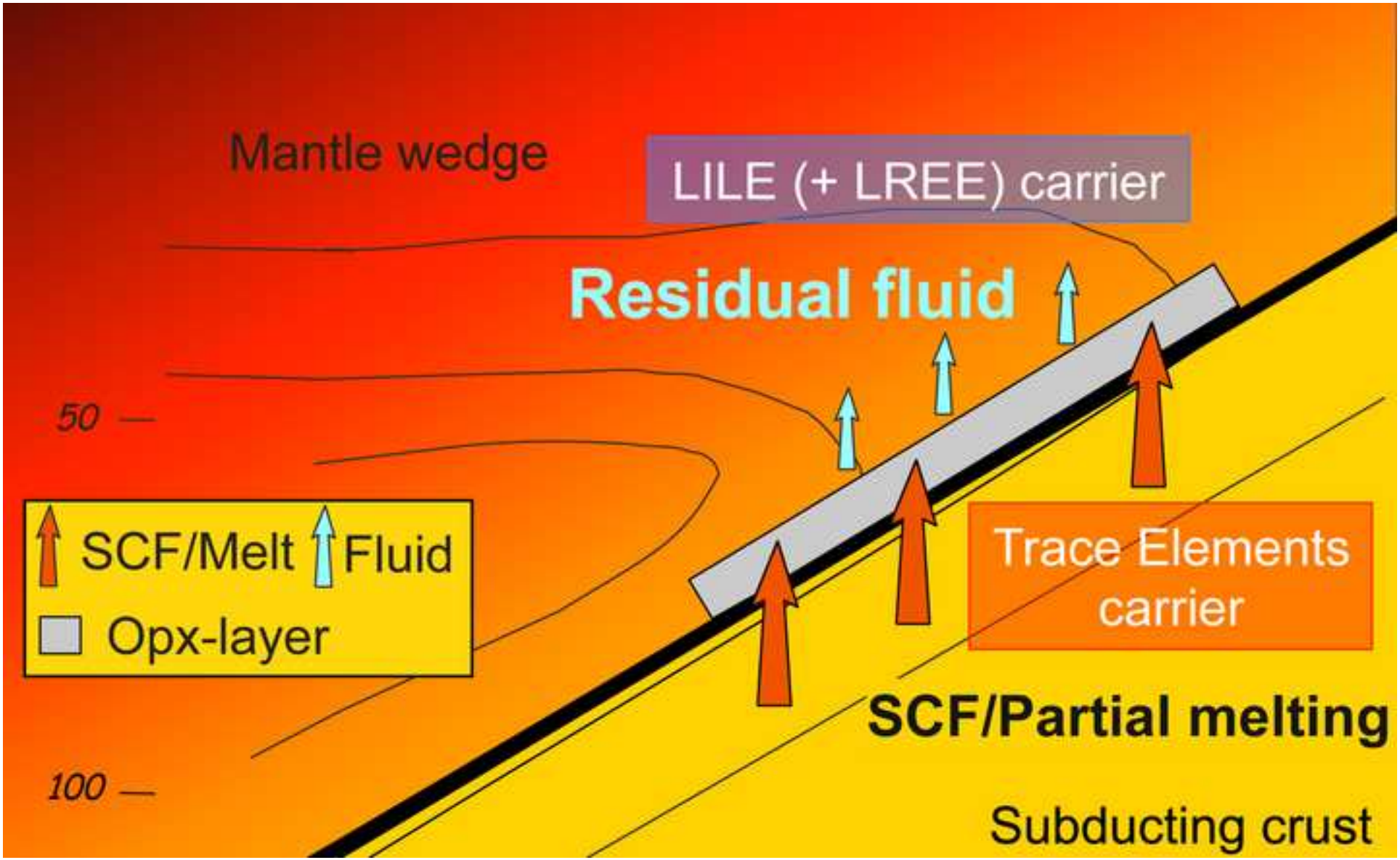

Figure 2

Click here to download high resolution image

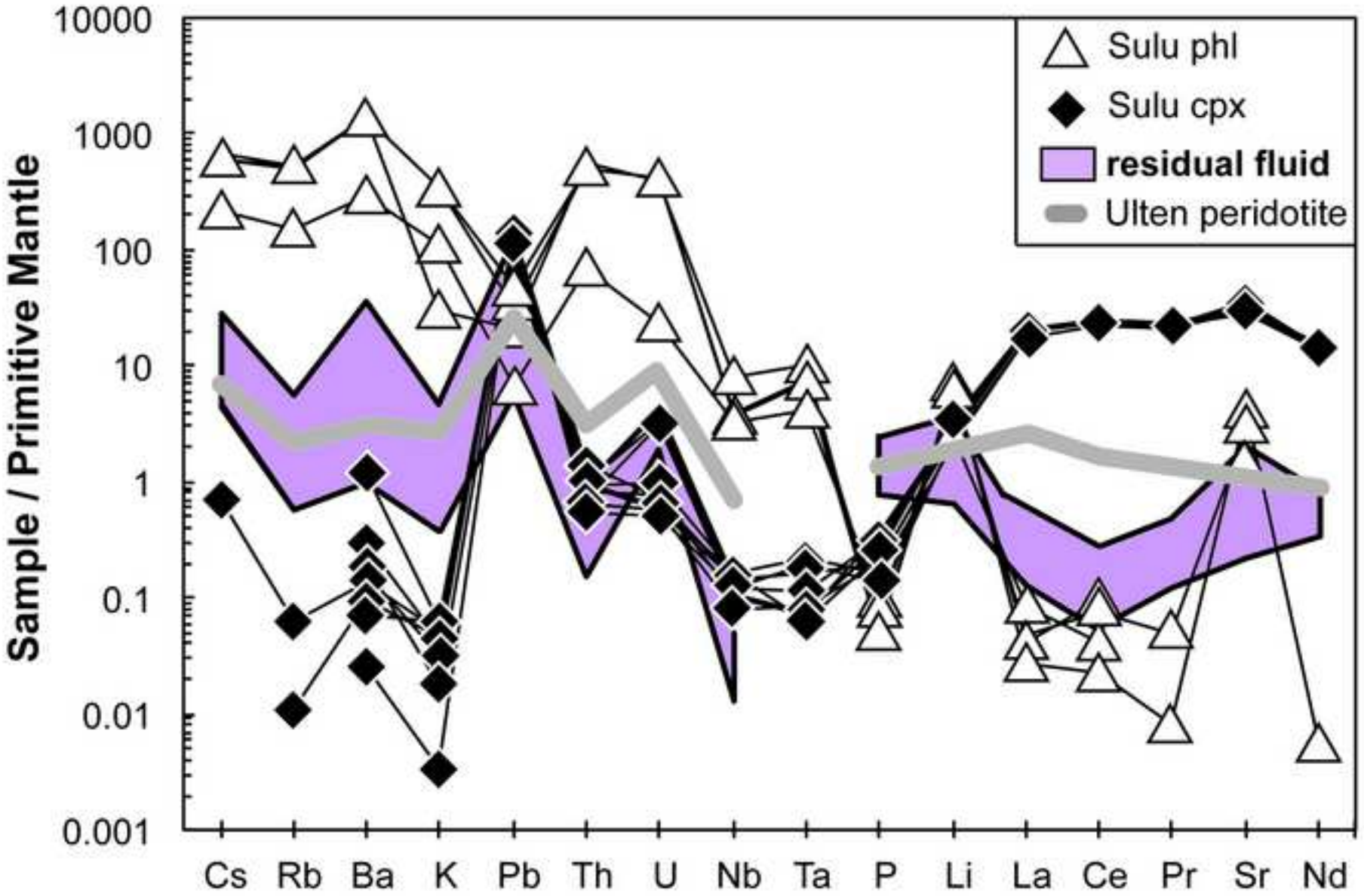

**Figure 3**

Click here to download high resolution image

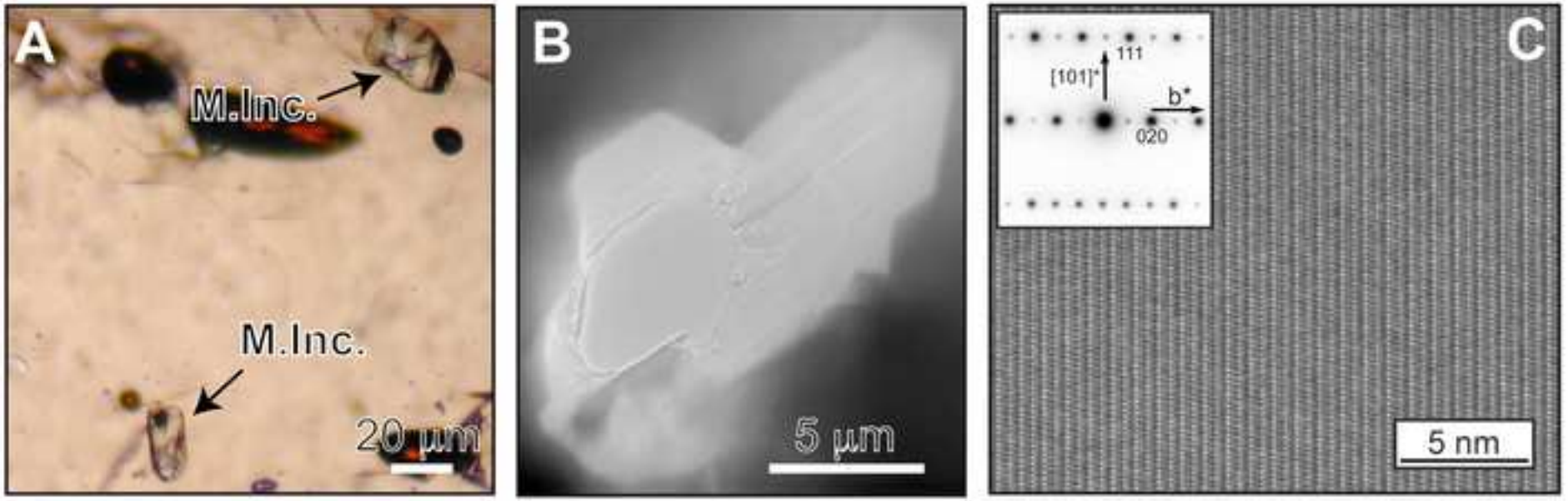

**Figure 4**

Click here to download high resolution image

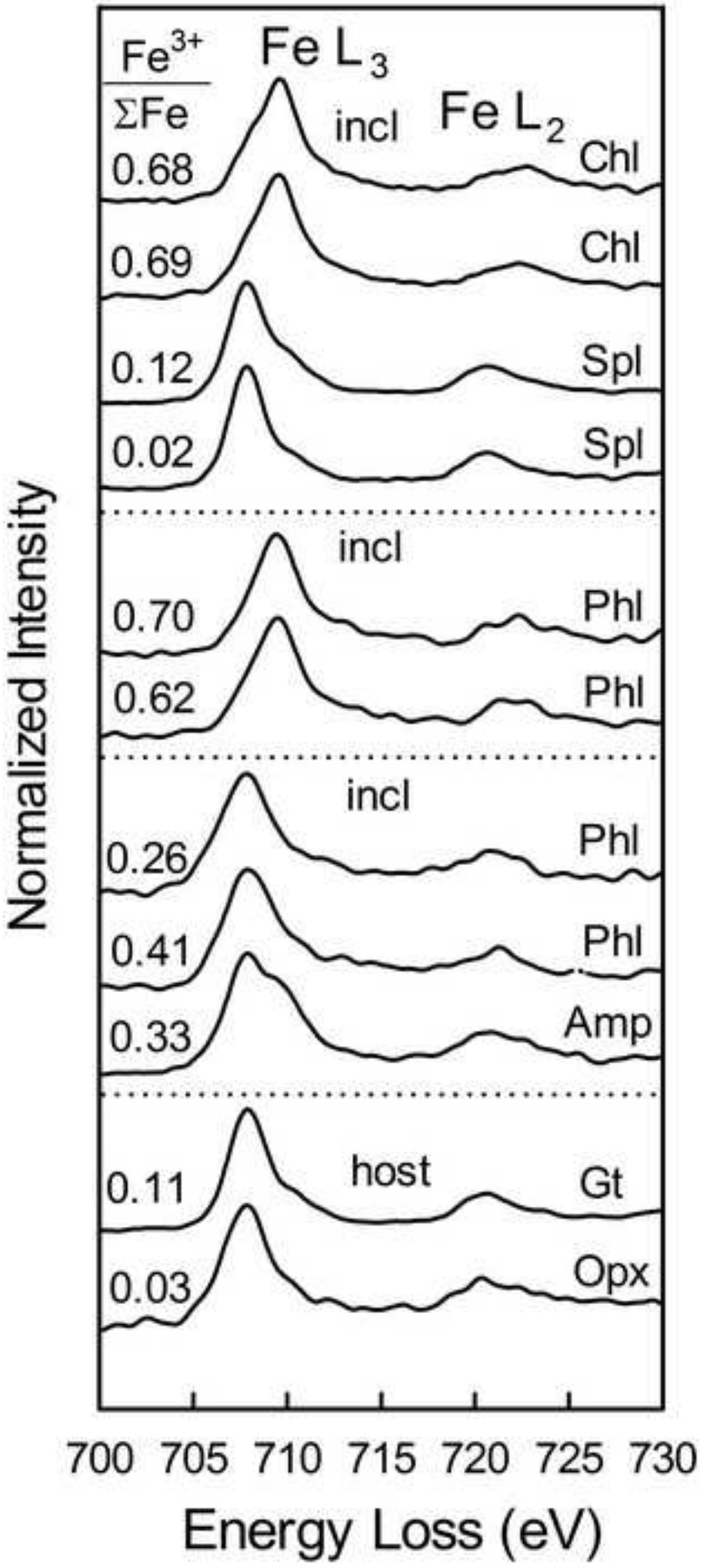

Figure 5

Click here to download high resolution image

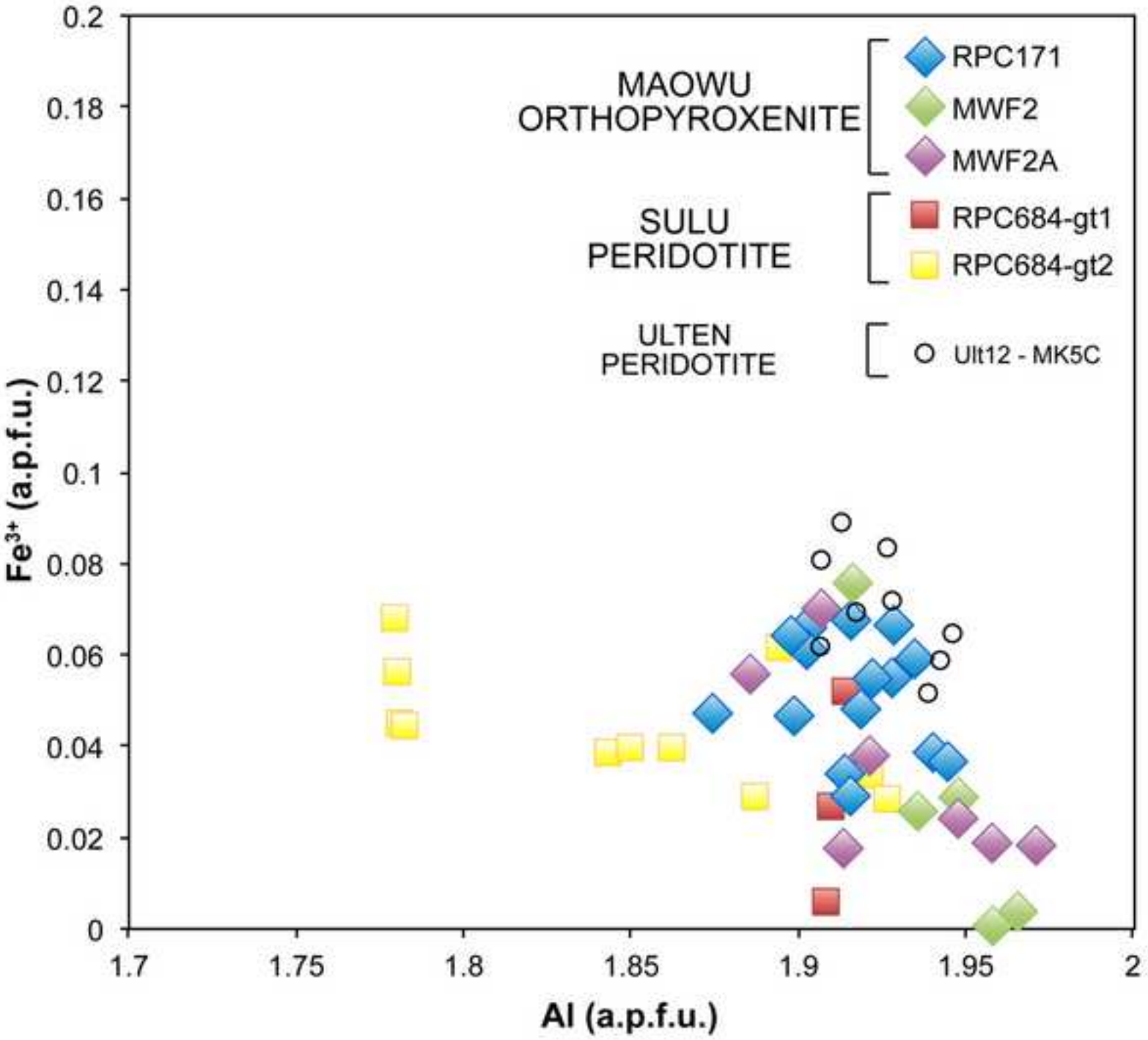

Figure 6

Click here to download high resolution image

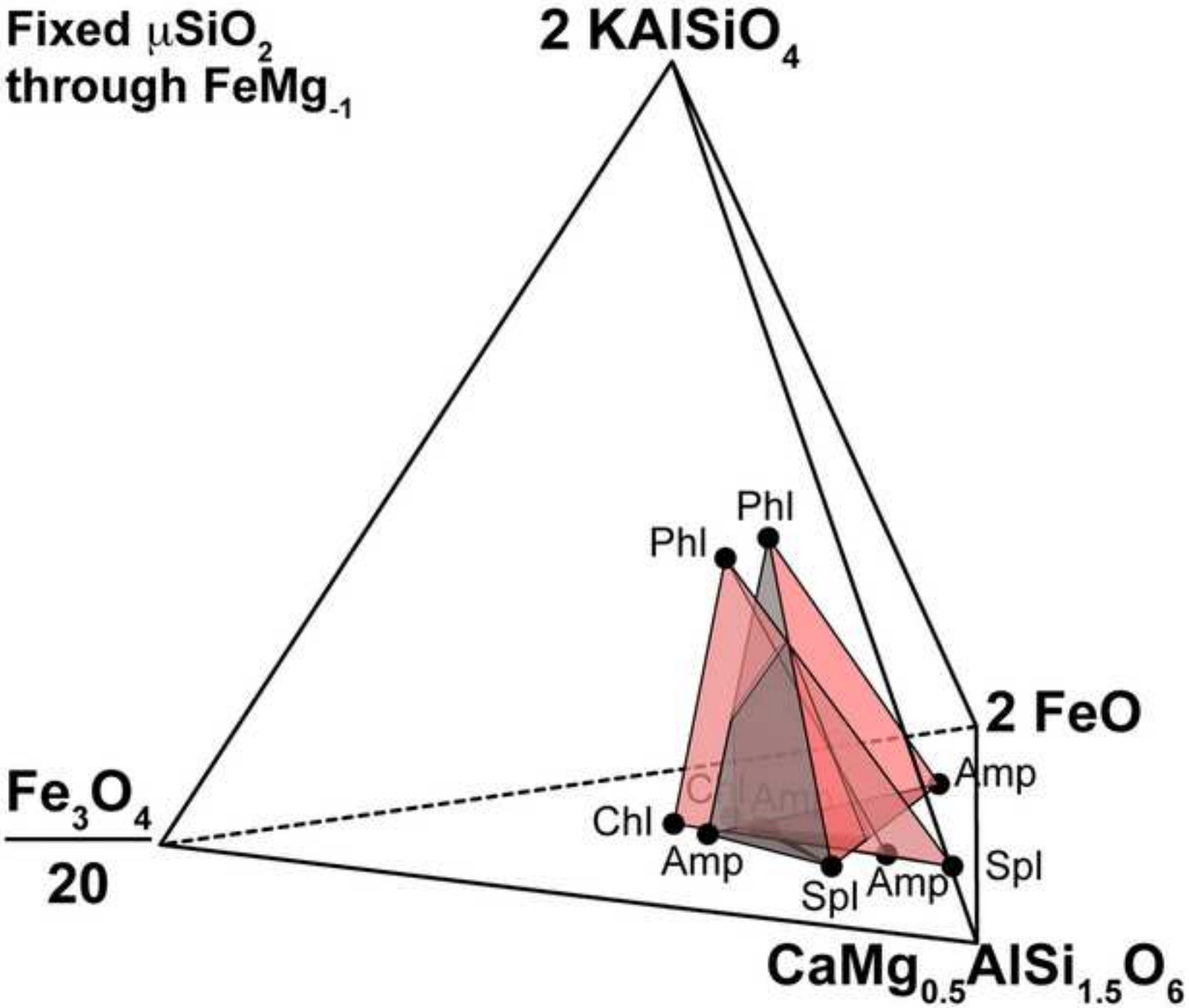

Figure 7

Click here to download high resolution image

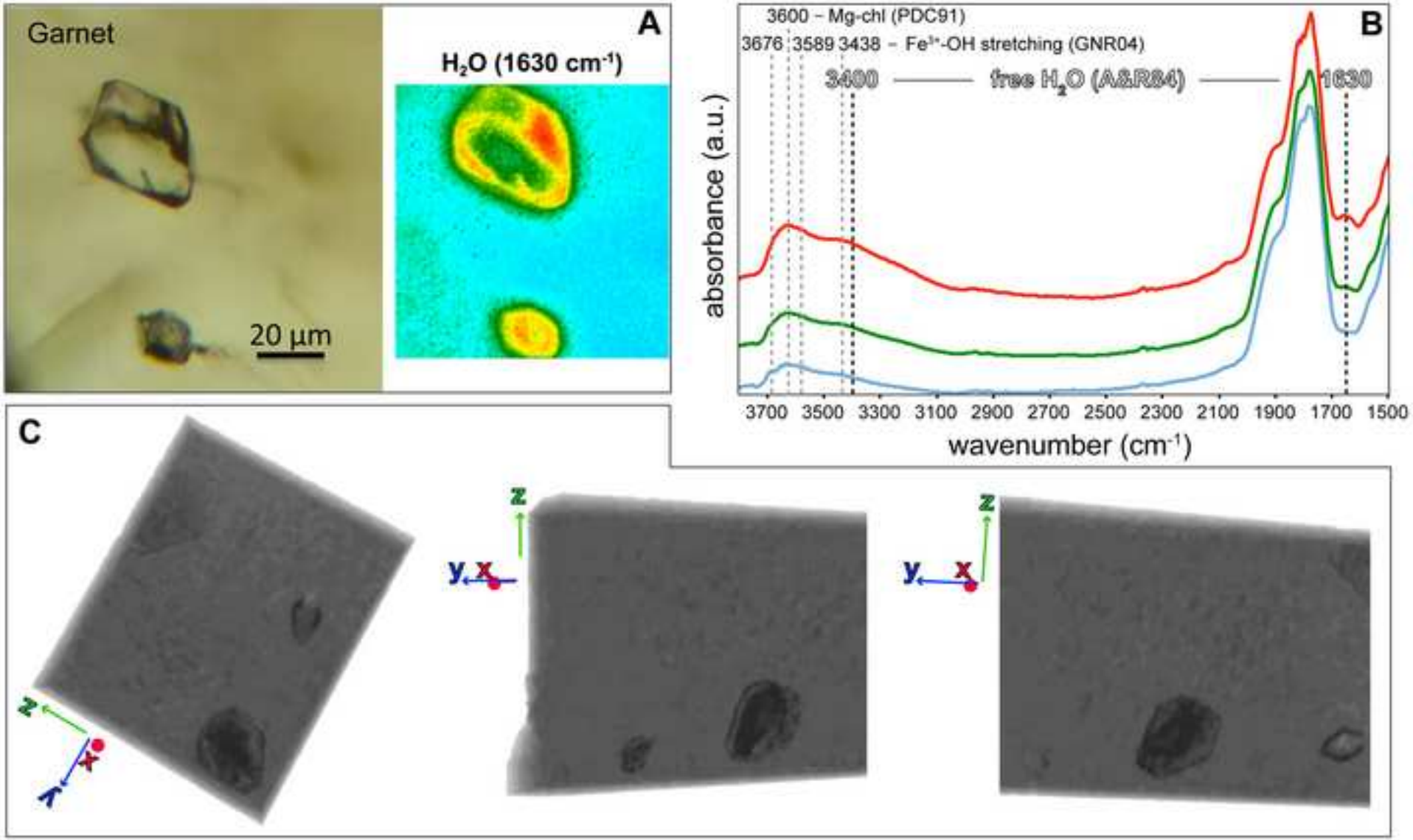

**Figure 8**

Click here to download high resolution image

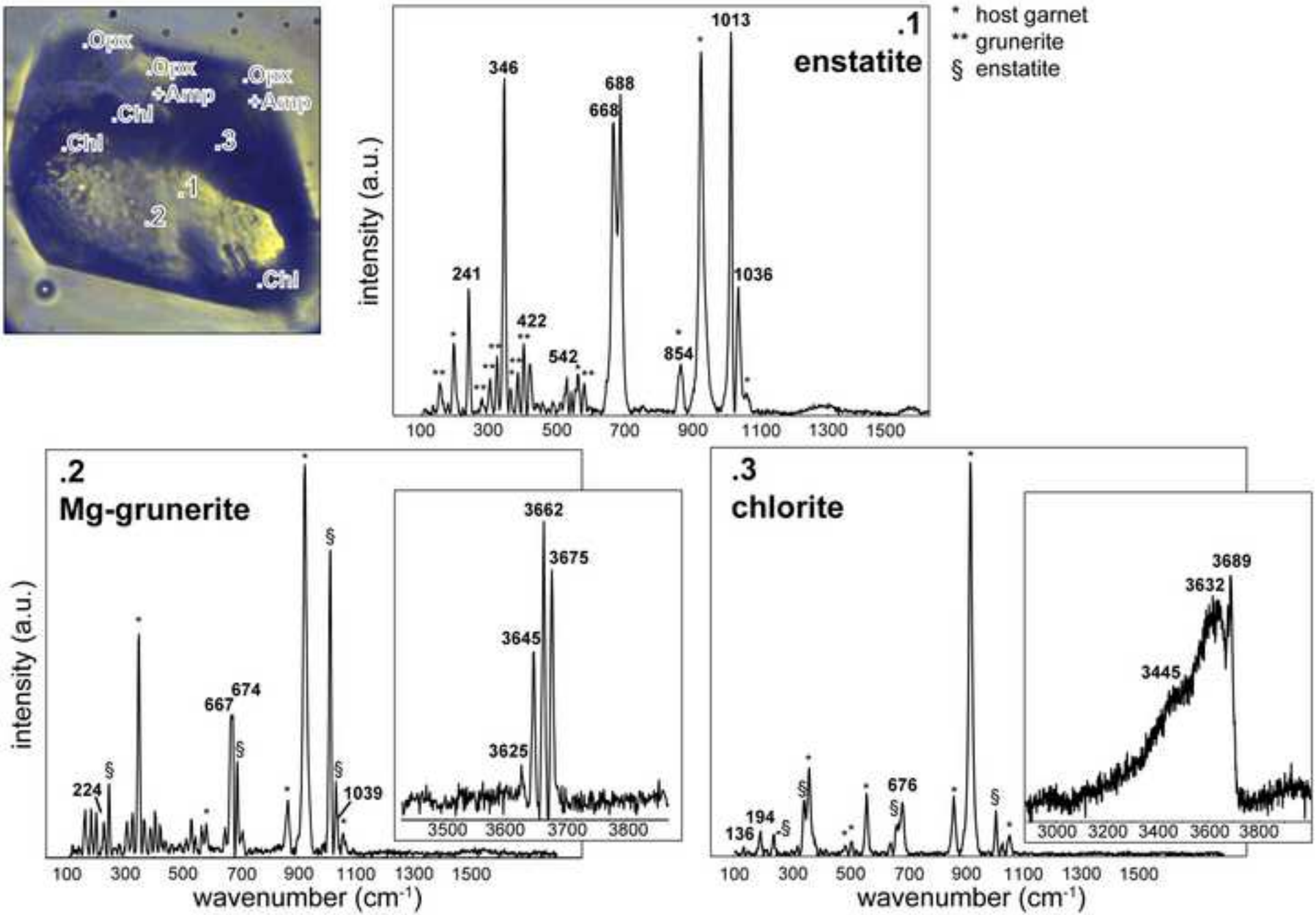

Figure 9

Click here to download high resolution image

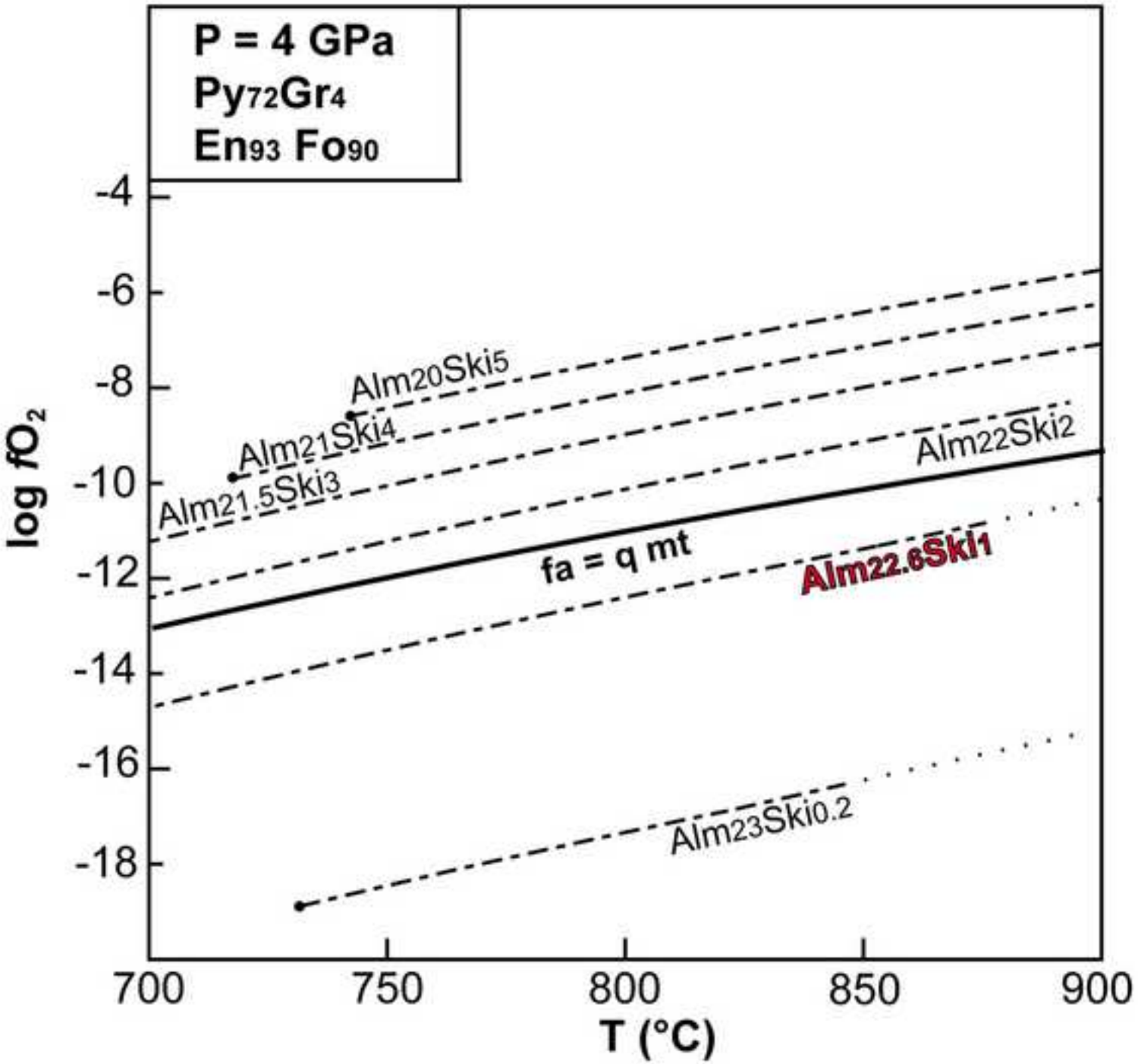

Figure 10

Click here to download high resolution image

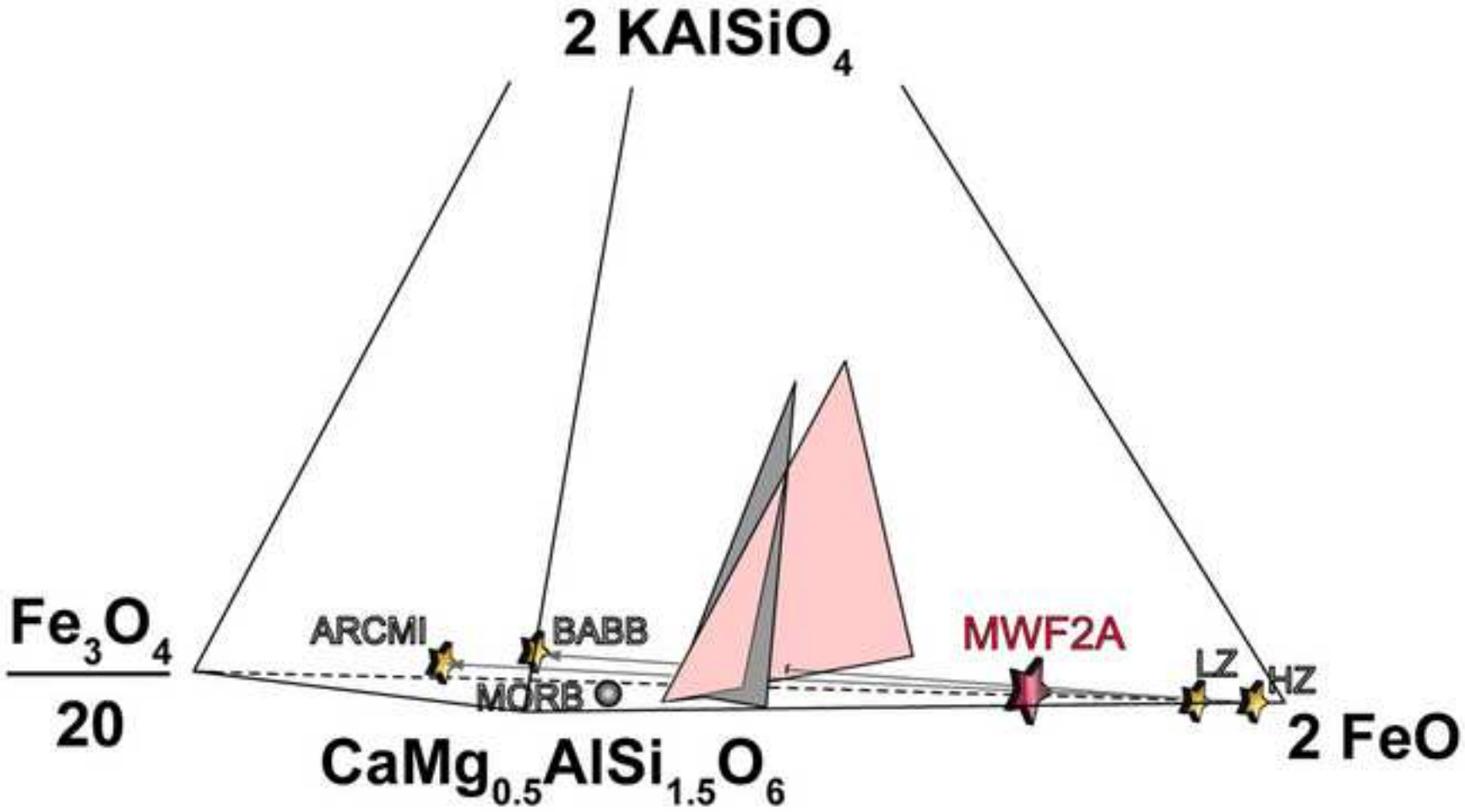

**Figure 11**

**Click here to download high resolution image**

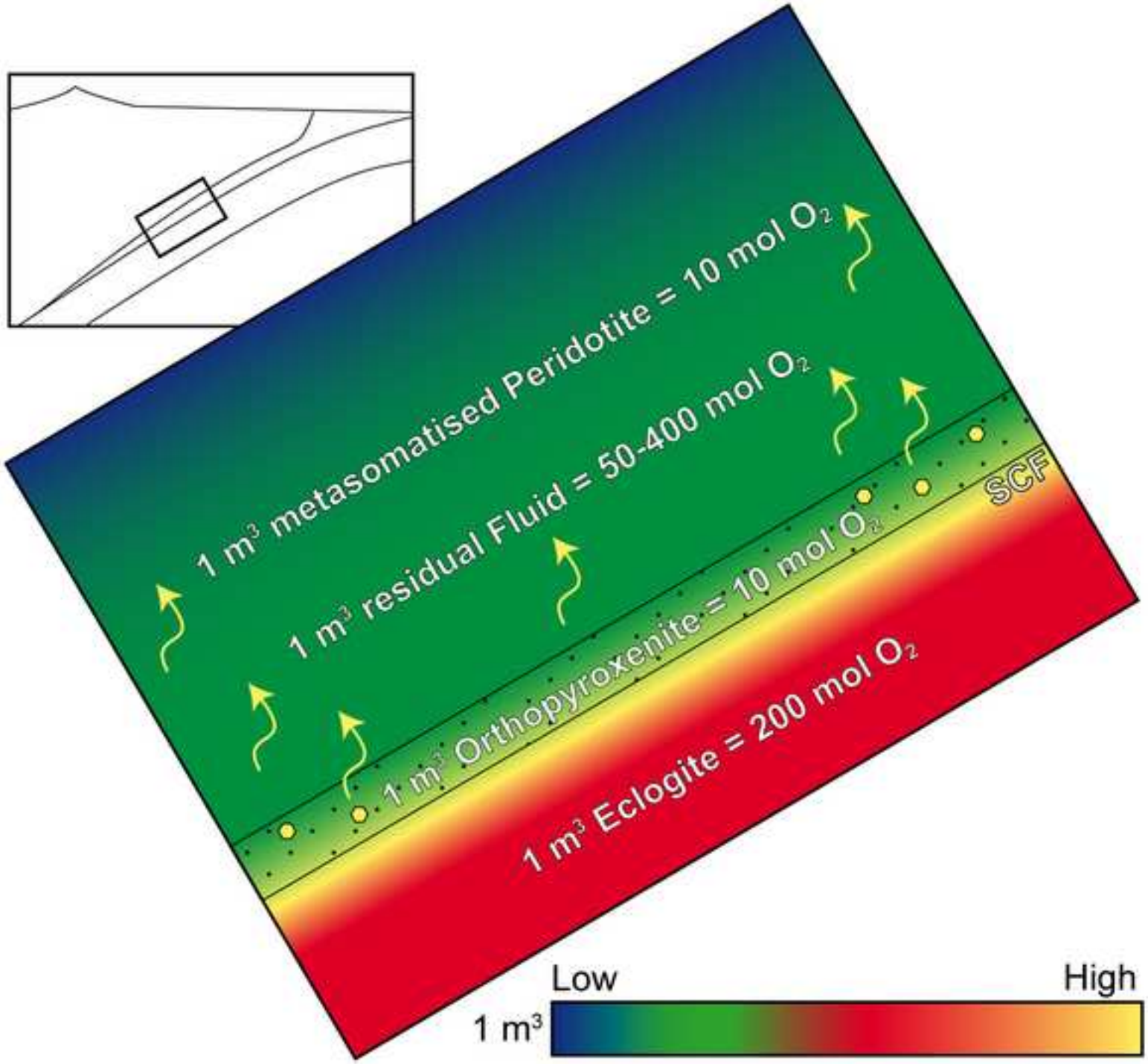

**LaTeX Source Files**

**Click here to download LaTeX Source Files: malaspinaetalgca.doc**

**Table 1**

**Click here to download LaTeX Source Files: Tab1.xlsx**